A boundary element method for microscopic Stokes flow in deep drawing processes

Brasjen, B.J.

Award date:
2008

A boundary element method for microscopic Stokes flow in deep drawing processes

B.J. Brasjen

August 2008

Abstract

A boundary element code has been developed for the calculation of the flow in microscopic two-dimensional domains. The code is based on a boundary integral formulation of Stokes flow, which is discretized and solved using an iterative solver. The code offers possibilities for extensions regarding the behavior and interactions of multiple fluids. These extensions are essential steps towards a microgeometry model of deep drawing friction, which is an important research topic for Corus RD&T and its clients in the automotive industry.

Special attention has been paid to the discretization of the geometry, calculation of the Green's functions and computation of singular integrals. The code has been validated using the flow between two flat, parallel walls in opposite motion, which has led to the theoretically expected result commonly known as Couette flow. In addition, calculations have been performed on a similar geometry with one of the walls being rough. The results from these calculations have proven to be numerically stable and to show expected behavior. Calculations on more complex geometries have not been successful as the iterative solver has not been able to find a convergence solution.

Contents

Chapter 1

Introduction

Friction, the opposition against the relative motion of two surfaces in contact [1], is one the most ubiquitous physical processes. Although it occurs in numerous types and forms, a general distinction is made between three types, based on the interacting objects: the friction of two solids is commonly referred to as dry friction, whereas fluid friction serves as the generic term for the friction between all kinds of gases and liquids [2]. Finally, the third type of friction comprehends the response of objects to deformation; this type of friction is generally called internal friction. The mechanism of internal friction is essentially identical to the former two: there are two surfaces opposing to an applied sliding motion. However, in case of internal friction, these two surfaces are part of the same object, e.g the object's surface and its bulk, whereas in case of dry and fluid friction, the two surfaces belong to different bodies.

Since friction is a dissipative mechanism, i.e. converting kinetic energy to thermal energy, it can cause damage to the objects in contact and it is therefore often desired to reduce the friction. Of a wide variety of friction reducing methods, lubrication is perhaps the most common. In lubrication, the friction is reduced by inserting a lubricant separating the two original contact surfaces, since a well-chosen lubricant naturally opposes less to motion. Among the most often used lubricants are not only liquids, such as oil or water, but also powdery solids, e.g. graphite. It is important to note that the ability to accurately reduce the friction in a certain process implies the ability to control the friction in this process. Controlling friction converts the risk of damage caused by friction to a benefit: the frictional mechanism can be used to smooth rough surfaces, for instance. Therefore, there is a lot of industrial interest in tribology, the science of lubrication and friction.

1.1 Present and future state of friction modeling

The continuous need for cost minimization and safety improvement in the automotive industry requires strict control of the thickness of the metals and thereby thorough understanding of sheet metal forming processes, in particular the deep drawing process, which is most generally used. In this process, a sheet of metal is clamped to a die by a blankholder, after which a punch is moved down at a constant velocity of the order of mm/s, thus forming the sheet. The magnitude of the clamping force of the blankholder determines to what extent the sheet can move and/or will be stretched. Obviously, the blankholder force can not be too small or too large, since this would decrease the quality of the product by wrinkling or rupture, respectively. A schematic drawing of the deep drawing process is shown in figure 1.1. As stated above, the quality of the product is mostly determined

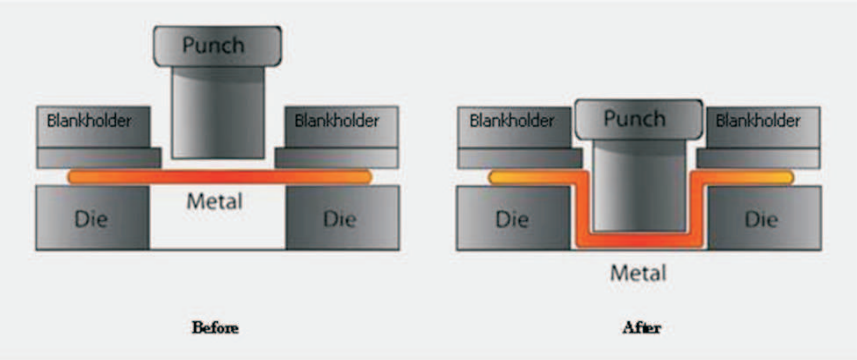

Figure 1.1: Sketch of the deep drawing process [3].

by the friction mechanism in the blankholder region. Therefore, in order to control the quality, the friction in this region has to be known very precisely. Currently available friction models use a macroscopic friction coefficient f to describe the friction, defined by

$$f = \frac{F_w}{F_{load}}, \tag{1.1}$$

in which F_w represents the macroscopic friction force and F_{load} represents the clamping force, also referred to as (normal) load or load force, exerted by the blankholder. As can be seen in figure 1.2, the load force is applied on the blankholder as a whole, whereas the die is simply kept at its place. The friction force is then the force of the entire workpiece opposing to its motion caused by the punching.

However, wrinkling and rupture can occur at very small scale, depending on local conditions. Therefore, it is necessary to determine the friction coefficient locally, thus incorporating local conditions in addition to the global

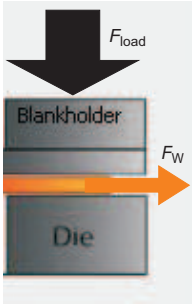

Figure 1.2: Macroscopic forces in the blankholder region.

conditions. These local conditions are mainly caused by the micrometer scale geometry [4] of both the blankholder and the sheet metal, which is shown in figure 1.3. Considering the deep drawing friction process at mi-

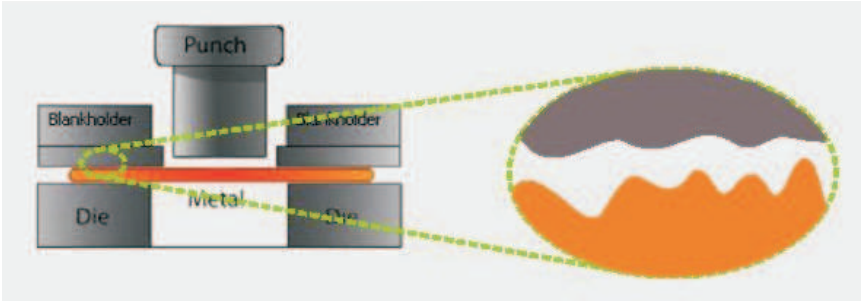

Figure 1.3: Micrometer scale view on the clamping region.

crometer scale converts the problem to a more general interaction between three components: a solid tool (in the case of deep drawing this is the blankholder), a lubricant (mostly oil in deep drawing) and a solid workpiece (the sheet of metal). It appears that the tool and the workpiece, though macroscopically flat, have rough surfaces on a micrometer scale. In industrial deep drawing processes, the tool roughness has a typical length scale of 10^{-4} m and a typical height scale of 10^{-7} m, whereas the workpiece roughnesses has typical dimensions of 10^{-5} m and 10^{-6} m, respectively [5]. As a consequence of the two roughness profiles, the amount of lubricant between the surfaces determines whether the two surfaces are in full, partial, or no contact, as can be seen in figure 1.4. The amount of lubricant depends on the hydrodynamic pressure, since this pressure prevents the lubricant from being squeezed out of the system. Naturally, the contact between tool and surface causes more friction than the lubricated contact. Therefore, three different friction regimes can be distinguished, depending on the relative

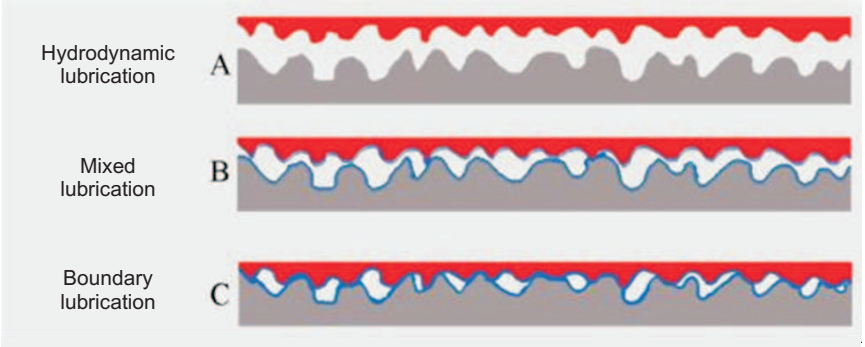

Figure 1.4: Schematic representation of the three lubrication regimes.

area of contact between tool and workpiece. First, if the dominating type of contact is the contact between the tool and the workpiece, the system is in the boundary lubrication regime, denoted C in figure 1.4. The name, commonly abbreviated to BL, originates from the boundary layers that are chemically adsorbed to the solid surfaces and determine the shear strength of the contact surface and thereby the friction. Since this shear strength is mostly 10 to 100 times larger than the shear strength of the solid to fluid contact and the solid to solid contact is the dominating type on the contact surface, the influence of the lubricant is negligible in the boundary lubrication regime. The opposite of boundary lubrication is commonly referred to as hydrodynamic lubrication (abbreviated to HL), which is a regime in which the tool and the workpiece are fully separated by the lubricant. The friction is then determined by the viscous shear strength of the lubricant, leading to friction coefficients of 10^{-3} to 10^{-2}, which are significantly smaller values than the 10^{-1} generally occurring in the BL regime. A sketch of a contact in hydrodynamic lubrication can be seen in figure 1.4, part A. Finally, part B shows the intermediate regime, which occurs when a system undergoes a transition from boundary lubrication to hydrodynamic lubrication. In this regime, the areas of the solid to solid contact and the solid to lubricant contact are of the same order of magnitude, leading to intermediate values of the friction coefficient. The obvious name of this regime is mixed lubrication, or ML.

In 1902, the German engineer Richard Stribeck captured the influence of the three most important experimental parameters in one curve, by plotting experimental values of the friction coefficient f against the Hersey parameter, defined by

$$He = \frac{\eta V}{p_{nom}}, \tag{1.2}$$

with η representing the dynamic viscosity of the lubricant, V representing the relative velocity of the tool and the workpiece and p_{nom} representing

the load pressure, which is the clamping force divided by the total area of the blankholder. From (1.2), it can be seen that both the lubricated friction contribution (dependent on η and V) and the ratio between solid to solid contact area and solid to lubricant contact area (dependent on V and p_{nom}, the two parameters determining the balancing between the velocity dependent hydrodynamic pressure generated by the motion and applied pressure) are represented in the parameter, which thereby captures the most important experimental conditions of the friction process.

The Hersey parameter has the dimension [m] and therefore, Schipper [6] suggested the use of the dimensionless lubrication number Lu, defined by

$$Lu = \frac{\eta V}{p_{nom} Ra_w},, \tag{1.3}$$

with Ra_w the average roughness of the workpiece, which is by definition given by

$$Ra_w = \frac{1}{L} \int_0^L \mid y_w(x) \mid dx. \tag{1.4}$$

In (1.4), y_w represents the local height of the roughness. Since the roughness is random, integration in one, also random direction provides an accurate measure of the average roughness of the workpiece, as long as the length of the integration interval is much larger than the typical roughness height scale H,

$$\frac{H}{L} \ll 1. \tag{1.5}$$

Considering expression (1.2) and figure 1.4, the influence of the lubricant on the friction becomes apparent, as a smaller applied pressure p_{nom} implies a larger amount of lubricant and thus a larger separation of tool and workpiece, which decreases the friction. Moreover, a larger V, causing more hydrodynamic pressure and thus more tool lifting, lowers the friction as well. For larger values of the Hersey parameter (or the lubrication number), the system is in the HL regime, implying a viscous stress dominated friction coefficient. The He intervals corresponding to the different lubrication regimes strongly depend on the chosen materials. Since the viscous stress is a linear function of the vertical gradient of the horizontal velocity, a larger horizontal velocity, as well as a smaller roughness scale, causes an increase of the viscous stress and thereby the friction coefficient, the latter by decreasing the typical separation distance between the two metals. This implies that at the same contact area ratio, the typical heights of the lubricant channels are smaller, but the horizontal velocity difference is not, thus leading to increasing gradients.

As can be seen in figure 1.5, the three lubrication regimes can be clearly distinguished in the Stribeck curve. According to figure 1.5, most deep drawing processes are in the BL and the ML regimes. Present models enable accurate friction calculation for the BL regime [3], the mixed lubrication

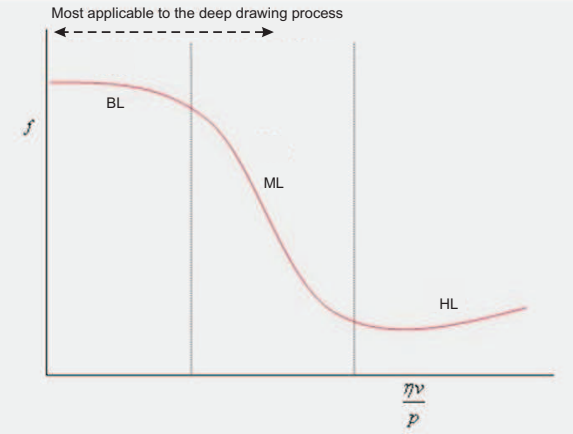

Figure 1.5: Typical example of a Stribeck curve showing the distinction between different lubrication regimes.

however has so far proven to be far more difficult to capture in an accurate model [5]. Since the mixed lubrication process is composed of a BL component and an HL component, the obvious first step towards an ML model is to study the hydrodynamic part of the mixed lubricated process.

1.2 Numerical methods in friction modeling

As stated before, the majority of present day friction models is based on macro geometry effects. Models including micro geometry effects show limited possibilities as a consequence of calculation times. The current Corus micro geometry model originally considered only frictional processes in the boundary lubrication regime [3] and used height distribution functions of the surface's roughnesses. These distributions were fitted to enable their use in analytically evaluated integrals based on a metal deformation model developed by J.D. Westeneng [4]. The extension of this model towards mixed lubricated processes, by filling the voids between the metals with lubricant and implementing the fluid behavior into the original boundary lubrication integral equations, revealed some serious problems, especially in the field of modeling the relative influences of the different aspects of the entire frictional process (i.e. metal to metal sliding friction, metal to lubricant sliding friction, metal deformation, lubricant pressure generation, et cetera) accurately [5].

The numerical problems that have arisen during the development of the current Corus micro geometry model have prompted the development of a new model, based on a different approach. This new model will capture the three main process components into one set of equations, based on the

behavior of the lubricant between two rigid walls. In the future, the tool and workpiece deformation can be incorporated by modeling these metals as highly viscous, Newtonian fluids. Modeling all process components as fluids reduces the complexity of the model, since only fluid behavior has to be incorporated. Moreover, all process components can be modeled simultaneously, so problems adjusting the relative influences of the different parts of the process after calculating them separately should be avoided.

The setup of this three-fluid model will be based on a boundary element method [7] [8] for viscous flow governed by the Stokes equations. This method, enabling calculating the behavior of a volume from the behavior of its bounding surface, reduces the dimension of the problem by one. Obviously, this reduction leads to a significant decrease in memory usage.

1.3 Outline of the thesis

This section provides a global overview of the content of the remaining chapters. In chapter 2, the theoretical basis of the model will be discussed; the main focus will be on the derivation of the Stokes equations and the formulation of boundary conditions for the problems that will be modeled. Furthermore, an example of Stokes flow will be introduced and the integral solution of the Stokes equations for this problem will be derived. Chapter 3 is devoted to the derivation of the integral formulation of the Stokes equations, whereas chapter 4 focuses on the numerical methods developed to solve the integral equations. The validation of the code and the results of calculations on a single asperity geometry are discussed in chapter 5. Finally, the conclusions and future prospectives can be found in chapter 6.

Chapter 2

Theory of Stokes flow

In this chapter, the deep drawing process will be reduced to a less complex problem in section 2.1, which will be shown to satisfy the Stokes equations in the second section. In section 2.2, the Stokes equations will be rewritten to describe the specific problem in the third section and boundary conditions will be derived for the problem, thus obtaining a full set of equations and boundary conditions. Finally, the two-dimensional equations as well as an analytical solution to these equations are derived, following [9], in section 2.3.

2.1 Problem definition

In order to find a simple, yet accurate characterization of the deep drawing process, several assumptions need to be made regarding all three process components, as has been discussed in the previous chapter. The tool, first of all, is assumed to be infinitely hard and smooth, implying that it can be considered a rigid wall that can not be affected by any of the other components. The workpiece, on the other hand, can be rough, but is also assumed to be rigid initially. Thus, its roughness peaks, often referred to as asperities, will affect the flow of the lubricant, but deformation of the peaks can not occur. Finally, the lubricant is assumed to be a Newtonian fluid with a constant density and viscosity.

As a first, simple approximation of the workpiece geometry, a two-dimensional box containing a certain amount of lubricant bounded by the tool and the workpiece is chosen. The workpiece is assumed to have exactly one asperity within the boundaries of the box. A two-dimensional representation of the box problem is shown in figure 2.1. In figure 2.1 it can be seen that the workpiece and the tool will be regarded as boundaries; bulk deformation, which can occur outside these boundaries in practice, will not be incorporated. The process of deep drawing has now been reduced to a two-dimensional thin film flowing in a narrow and rigid channel, with one

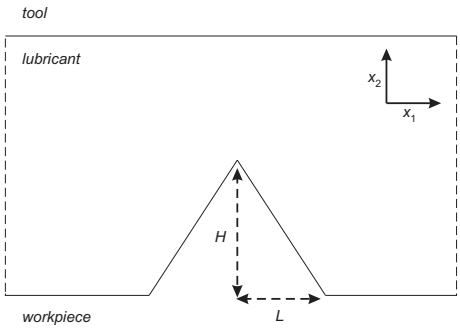

Figure 2.1: Schematic representation of the two-dimensional deep drawing problem.

wall being smooth and the other containing one disturbance.

2.2 Governing equations

The behavior of the lubricant is governed by the continuity equation and the Navier-Stokes equation. The first equation guarantees the conservation of mass, whereas the latter incorporates all quantities involved with momentum conservation. The continuity equation reads

$$\partial_t \rho + \partial_i \left(\rho u_i\right) = 0, \tag{2.1}$$

with ρ representing the density of the fluid and u_i representing the velocity field, with $i = 1, 2, 3$ in case of three-dimensional problems. In (2.1) and henceforth, the Einstein summation convention is adopted, which means summation over repeated indices. In addition, an abbreviated representation for derivatives is introduced, yielding the following notations:

$$\begin{aligned} \partial_t &= \frac{\partial}{\partial t}, \\ \partial_i &= \frac{\partial}{\partial x_i}, \\ \partial_{ij} &= \frac{\partial^2}{\partial x_i \partial x_j}, \end{aligned} \tag{2.2}$$

For an incompressible fluid, which is characterized by a uniform and constant density, equation (2.1) reduces to

$$\partial_i u_i = 0. \tag{2.3}$$

This means that the velocity field is divergence free.

The Navier-Stokes equation then reads

$$\partial_t u_i + (u_j \partial_j)\, u_i = -\frac{1}{\rho}\partial_i p + \frac{\mu}{\rho}\partial_{jj} u_i + f_i. \tag{2.4}$$

It should be noted that it is a vector equation, consisting of three components, one for each dimension. The pressure is represented by p and μ represents the dynamic viscosity of the lubricant. On the extreme right of equation (2.4), f_i represents the sum of body forces per unit mass. In the absence of externally applied body forces, this expression is equal to the gravitational acceleration g, which has only a component in the vertical direction.

2.2.1 Stokes flow

The Navier-Stokes equation can be simplified by performing a scale analysis, using typical values for the relevant quantities. These typical values, based on the practice of deep drawing, have been mentioned briefly in the previous chapter. The length and height scales are taken from the typical dimensions of the workpiece, whereas the typical velocity is taken from the velocity of the punch. From this typical velocity and length scale, U and L respectively, a typical time scale T can be defined as the ratio of L and U. By replacing all the quantities on the left-hand side of the Navier-Stokes equation by their scale equivalent, an estimation of both terms can be found.

$$|\partial_t u_i| + |(u_j \partial_j)\, u_i| \approx \frac{U}{T} + U\frac{U}{L} = \frac{U^2}{L} + \frac{U^2}{L}. \tag{2.5}$$

The time-dependent term and the convective term thus prove to be of equal order of magnitude. Therefore, it is sufficient to compare only one of these terms to the terms on the right-hand side. First of all, the gravitation is found to be roughly of the same order as the convective term,

$$\frac{|g|}{|(u_j \partial_j)\, u_i|} \approx \frac{g}{\frac{U^2}{H}} = \frac{Hg}{U^2} \approx \frac{10^{-6} \cdot 10^1}{10^{-6}} = 10^1. \tag{2.6}$$

In (2.6), the typical height H is used instead of the typical length L, since the gravity has only a vertical component to compare with other terms. As can be seen in figure 1.4, the separation distance between the tool and the workpiece is of the same order of magnitude as the typical roughness height. It is convenient to express (2.6) in dimensionless numbers, which characterize the flow in a more general way. In the case of equation (2.6), the dimensionless number comparing gravity to convection, is known as the Richardson number, defined by

$$Ri = \frac{Hg}{U^2}. \tag{2.7}$$

Since $Ri \approx 10^1$, the gravitational term can only be neglected if the convective term is found to be negligible as well. The pressure gradient is unknown, so the convective term on the left-hand side will be compared to the viscous term on the right-hand side. The ratio of these two terms is given by the Reynolds number

$$\frac{|(u_j \partial_j)\, u_i|}{\left|\frac{\mu}{\rho}\partial_{jj} u_i\right|} \approx \frac{\frac{U^2}{L}}{\frac{\mu}{\rho}\frac{U}{L^2}} = \frac{\rho U L}{\mu} = Re. \tag{2.8}$$

The magnitude of the Reynolds number can be evaluated by filling in the typical experimental values $\rho \approx 10^0 \text{kgm}^{-3}$, $\mu \approx 10^{-1}\text{Pas}$, $U \approx 10^{-3}\text{ms}^{-1}$ and $L \approx 10^{-5}\text{m}$, using the length scale of the workpiece, since the tool roughness is neglected. The practical values give a Reynolds number of the order of 10^{-7}, which implies that the terms on the left-hand side, and thereby also the gravitational term, can be neglected. Using a typical height scale H (in the order of 10^{-6} for the workpiece) instead of L decreases the Reynolds number with an additional factor 10.

The magnitude of the pressure gradient can be estimated using the Reynolds equation for hydrodynamic pressure [10],[11], which leads to

$$\frac{1}{\rho}\partial_i p \approx \frac{\mu U}{\rho L^2}, \tag{2.9}$$

which is exactly the same expression as the estimation of the viscous term. Since all terms on the left-hand side as well as the gravitational term on the right-hand side are negligible compared to the viscous term, the viscous term must then be equalled by the pressure gradient, leading the Navier-Stokes equation to reduce to the Stokes equation, given by

$$0 = -\partial_i p + \mu \partial_{jj} u_i. \tag{2.10}$$

The pressure term and the viscous term are often represented together by the Newtonian stress tensor σ, of which the ij-component is defined as

$$\sigma_{ij} = -p\delta_{ij} + \mu\left(\partial_j u_i + \partial_i u_j\right), \tag{2.11}$$

leading to an equivalent form of the Stokes equation,

$$0 = \partial_j \sigma_{ij}. \tag{2.12}$$

From equation (2.12) it follows that in a Stokes flow the Newtonian stress tensor, like the velocity field, is divergence free at all times and under all boundary conditions. The omission of the time derivative in the Stokes equation does not imply that the flow is steady: the time dependence of the flow is governed by the time dependent behavior of the boundary conditions.

2.3 Two-dimensional equations

Applying the incompressible continuity equation (2.3) and the Stokes equation (2.10) to the two-dimensional problem of section 2.1, the following set of equations can be derived

$$\partial_1 u_1 + \partial_2 u_2 = 0 \tag{2.13}$$

and two components of the Stokes equation,

$$-\partial_1 p + \mu \left(\partial_{11} u_1 + \partial_{22} u_1\right) = 0 \tag{2.14}$$

and

$$-\partial_2 p + \mu \left(\partial_{11} u_2 + \partial_{22} u_2\right) = 0. \tag{2.15}$$

These are three equations for three unknowns: u_1, u_2 and p. In order to solve this set of equations, boundary conditions need to be formulated, which can be motivated from the problem definition from section 2.1. Applying the no-slip condition to the upper and lower boundary leads to velocity boundary conditions, whereas at the inlet and outlet of the box, i.e. the open boundaries at the left and right of figure 2.1, the pressure is assumed to be equal to an applied reference pressure, which can be set to zero since the Stokes equation only involves a pressure gradient. Overall, the boundary conditions are:

$$x_2 = -H \quad : \quad u_1 = -U, u_2 = 0 \tag{2.16}$$

$$x_2 = H \quad : \quad u_1 = U, u_2 = 0 \tag{2.17}$$

$$x_1 = -L \quad : \quad p = p_0 = 0 \tag{2.18}$$

$$x_1 = L \quad : \quad p = p_0 = 0. \tag{2.19}$$

The velocities on the left and right boundary are unknown. However, if these boundaries were at infinite distance or if the bottom wall were perfectly flat, the boundary velocities satisfy the Couette profile, which will be discussed in the next section. A sketch of the problem, including the boundary conditions, is shown in figure 2.2.

2.3.1 Couette flow

In the case of a flow induced by the opposite motion of two flat walls, both infinitely long, an analytical solution to the Stokes equations can be derived. A segment of the infinitely long channel and the boundary conditions are displayed in figure 2.3. As the length of the two walls is assumed to be infinite, there can be no dependence on the length coordinate x_1, implying $\partial_1 \phi = 0$, in which ϕ can be any of the relevant quantities u_1, u_2 or p. Substituting this in the continuity equation yields

$$\partial_2 u_2 = 0, \tag{2.20}$$

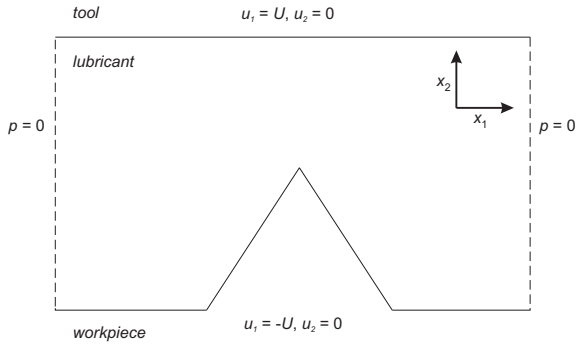

Figure 2.2: Two-dimensional box with boundary conditions.

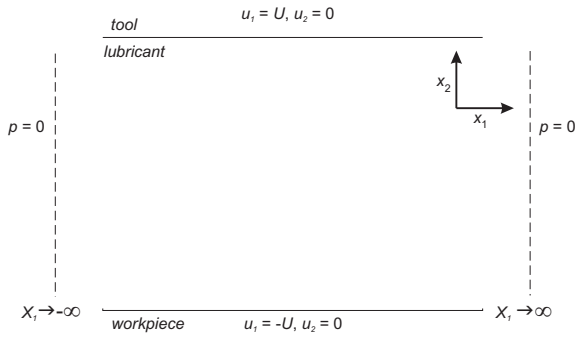

Figure 2.3: Boundary conditions for Couette flow.

implying that u_2 is a constant. Given the boundary conditions on the top and bottom wall, this means that $u_2 = 0$ in the entire domain. A similar substitution can be performed on the horizontal Stokes equation, leading to

$$\mu \partial_{22} u_1 = 0, \tag{2.21}$$

which has the general solution

$$u_1 = C_1 x_2 + C_2, \tag{2.22}$$

with C_1 and C_2 representing constants that are determined by boundary conditions. The first result, $u_2 = 0$ can now be used to simplify the vertical Stokes equation, yielding

$$\partial_2 p = 0. \tag{2.23}$$

This implies that the pressure is also constant in the entire domain, and given the boundary conditions on the left and right boundary, this constant is zero.

Finally, (2.22), in combination with the top and bottom wall boundary conditions (2.16) and (2.17), leads to an expression for the horizontal velocity,

$$u_1 = \frac{U}{H} x_2. \tag{2.24}$$

This can be used to calculate the stress tensor σ_{ij} using the constitutive equation (2.11), which is a function of the pressure and the velocity gradients. Since the only velocity gradient is $\partial_2 u_1$, the four components of the stress tensor reduce to

$$\begin{aligned} \sigma_{11} &= 0, \\ \sigma_{12} = \sigma_{21} &= \mu \frac{U}{H}, \\ \sigma 22 &= 0. \end{aligned} \tag{2.25}$$

With (2.24) and (2.25), the velocity and stress can be calculated for any point on the boundary of the domain, providing boundary conditions for both the velocity and stress. Thus, the Couette problem is can be readily used as a benchmark test for the new code, which will be done in chapter 5.

Chapter 3

Boundary integral formulation

In the first section of this chapter, an integral solution to the Stokes equations will be derived. Subsequently, a boundary integral formulation for this solution will be derived, closely following [12], [13],[7] and [8]. This formulation will serve as the basis for the computational model that will be developed.

3.1 Analytical solution

The set of equations governing the flow in the box, consisting of (2.13), (2.14) and (2.15), henceforth referred to as the Stokes problem, can be solved analytically. The general solution can be obtained by using the Lorentz reciprocal theorem [12], which involves singular kernels as Green's functions [13],[8].

3.1.1 Green's method

As the stress tensor σ is divergence free, the theory of Green's functions yields that the Green's function τ for the stress tensor satisfies the singularly forced Stokes equation

$$\partial_j \tau_{ij} = \delta\left(\mathbf{x} - \mathbf{x}_0\right), \tag{3.1}$$

in which $\delta\left(\mathbf{x} - \mathbf{x}_0\right)$ represents the Dirac delta function. Using the specific properties of this function, the velocity field u_i can be expressed as a function of the Green's function,

$$u_i\left(\mathbf{x}_0\right) = \int u_i\left(\mathbf{x}\right) \delta\left(\mathbf{x} - \mathbf{x}_0\right) d\mathbf{x} = \int u_i\left(\partial_j \tau_{ij}\right) d\mathbf{x}. \tag{3.2}$$

This expression can be rewritten by deriving the Lorentz reciprocal relation for the problem. Using properties of differential operators, the product $u_i\left(\partial_j \tau_{ij}\right)$ can be used to find an integral solution to the Stokes equations.

3.1.2 The Lorentz reciprocal theorem

Suppose there are two independent solutions to the Stokes equations: the first consists of u_i, p and σ_{ij}; the other consists of v_i, q and τ_{ij}. The latter set of variables is the solution known as singularly forced Stokes flow, implying

$$\partial_i v_i = 0 \tag{3.3}$$

and

$$-\partial_i q + \mu \partial_{jj} v_i = \delta\left(\mathbf{x} - \mathbf{x}_0\right), \tag{3.4}$$

which is equivalent to (3.1). Equations (3.3) and (3.4) will henceforth be referred to as the singularly forced problem. From Green's method, as discussed in the previous section, it follows that the product of u_i and τ_{ij} should be considered. As the two solutions are independent, the product of v_i and σ_{ij} should also be taken into consideration. The latter dot product reads

$$v_i \partial_j \sigma_{ij} = \partial_j \left(v_i \sigma_{ij}\right) - \sigma_{ij} \partial_j v_i. \tag{3.5}$$

Substituting the definition of σ into this identity gives

$$\begin{aligned} v_i \partial_j \sigma_{ij} &= \partial_j \left(v_i \sigma_{ij}\right) - \left(-p\delta_{ij} + \mu\left(\partial_j u_i + \partial_i u_j\right)\right) \partial_j v_i \\ &= \partial_j \left(v_i \sigma_{ij}\right) + p \partial_i v_i - \mu\left(\partial_j u_i + \partial_i u_j\right) \partial_j v_i. \end{aligned} \tag{3.6}$$

The term containing p equals zero due to the continuity equation (3.3). By interchanging the two flows, a similar relationship can be obtained:

$$u_i \partial_j \tau_{ij} = \partial_j \left(u_i \tau_{ij}\right) - \mu\left(\partial_j v_i + \partial_i v_j\right) \partial_j u_i. \tag{3.7}$$

By subtracting ((3.7)) from ((3.7)), the viscous term can be eliminated, leading to

$$v_i \partial_j \sigma_{ij} - u_i \partial_j \tau_{ij} = \partial_j \left(v_i \sigma_{ij} - u_i \tau_{ij}\right). \tag{3.8}$$

This relation will be used to derive the integral solution in the next section.

3.1.3 Green's functions

Let u_i, p and σ be the solution to the Stokes problem and v_i, q and τ the solution to the singularly forced problem. Then, the Stokes equation and continuity equation can be formulated for the Green's functions, yielding

$$\mu \partial_{jj} v_{ik}\left(\mathbf{x}, \mathbf{x}_0\right) - \partial_i q_k\left(\mathbf{x}, \mathbf{x}_0\right) = \delta\left(\mathbf{x} - \mathbf{x}_0\right) \delta_{ik} \tag{3.9}$$

and

$$\partial_i v_{ik}\left(\mathbf{x}, \mathbf{x}_0\right) = 0, \tag{3.10}$$

in which v_{ik} is the Green's function for the velocity, q_k is the Green's function for the pressure and δ_{ik} is the Kronecker delta, which is defined by

$$\delta_{ik} = \begin{cases} 1 & \text{if } i = k \\ 0 & \text{otherwise} \end{cases} \tag{3.11}$$

Introducing $r_i = x_i - x_{0,i}$ as the distance between two points $\mathbf{x}$ and $\mathbf{x}_0$ and following Lorentz [12], Ladyzhenskaya [13] and Pozrikidis [8], the Green's functions are obtained using Fourier transforms and, for two-dimensional problems, are given by

$$v_{ik}(\mathbf{x}, \mathbf{x}_0) \equiv \frac{1}{4\pi\mu} J_{ik}(\mathbf{r}) = \frac{1}{4\pi\mu}\left(\delta_{ik} \ln r - \frac{r_i r_k}{r^2}\right) \tag{3.12}$$

and

$$q_k(\mathbf{x}, \mathbf{x}_0) = -\frac{1}{2\pi}\frac{r_k}{r^2}, \tag{3.13}$$

in which $r = |\mathbf{r}|$. In the case of a three-dimensional problem, the expressions slightly differ and are given by

$$v_{ik}(\mathbf{x}, \mathbf{x}_0) \equiv -\frac{1}{\mu} J_{ik}(\mathbf{r}) = -\frac{1}{8\pi\mu}\left(\frac{\delta_{ik}}{r} + \frac{r_i r_k}{r^3}\right) \tag{3.14}$$

and

$$q_k(\mathbf{x}, \mathbf{x}_0) = -\frac{1}{4\pi}\frac{r_k}{r^3}. \tag{3.15}$$

Substituting (3.12) and (3.13) into the constitutive relation (2.11), an expression for the stress tensor τ_{ij} can be calculated. This expression is represented as the kernel K_{ijk}, given by

$$K_{ijk}(\mathbf{x}, \mathbf{x}_0) = -\frac{1}{\pi}\frac{r_i r_j r_k}{r^4} \tag{3.16}$$

for two-dimensional problems and by

$$K_{ijk}(\mathbf{x}, \mathbf{x}_0) = -\frac{3}{4\pi}\frac{r_i r_j r_k}{r^5} \tag{3.17}$$

in the case of a three-dimensional flow. In the remainder of this chapter, only two-dimensional problems will be considered.

Expressions (3.12), (3.13) and (3.16) can be used, together with (3.8), to derive expressions for u_i, p and σ_{ij}.

3.2 Boundary integral formulation

By integrating the reciprocal relation (3.8) over a control area S, bounded by a closed contour Γ, an integral representation of the Lorentz reciprocal relation is obtained,

$$\iint_S \left(v_i \partial_j \sigma_{ij} - u_i \partial_j \tau_{ij}\right) dS = \iint_S \partial_j \left(v_i \sigma_{ij} - u_i \tau_{ij}\right) dS. \tag{3.18}$$

Using Gauss' divergence theorem, expression (3.18) can be rewritten as

$$\iint_S \left(v_i \partial_j \sigma_{ij} - u_i \partial_j \tau_{ij}\right) dS = \oint_\Gamma \left(v_i \sigma_{ij} - u_i \tau_{ij}\right) n_j d\Gamma, \tag{3.19}$$

in which n_j is the inward unit normal at Γ. Substituting (2.12) into (3.19) leads to

$$\iint_S \left(u_i \partial_j \tau_{ij}\right) dS = -\oint_\Gamma \left(v_i \sigma_{ij} - u_i \tau_{ij}\right) n_j d\Gamma, \tag{3.20}$$

which can be further simplified using (3.2), yielding

$$u_i\left(\mathbf{x}_0\right) = -\oint_\Gamma \left(v_i \sigma_{ij} - u_i \tau_{ij}\right) n_j d\Gamma. \tag{3.21}$$

With the use of the Green's functions (3.12) and (3.16), the velocity u_i can be written as a function of $\mathbf{x}_0$ in boundary integral form. Defining the boundary traction f_j as

$$f_j\left(\mathbf{x}\right) = \sigma_{jk}\left(\mathbf{x}\right) n_k\left(\mathbf{x}\right), \tag{3.22}$$

the velocity in a point $\mathbf{x}_0$ on the boundary is given by

$$u_i\left(\mathbf{x}_0\right) = \frac{1}{2\pi\mu} \oint_\Gamma \left[J_{ij}\left(\mathbf{x} - \mathbf{x}_0\right) f_j\left(\mathbf{x}\right) - K_{ijk}\left(\mathbf{x} - \mathbf{x}_0\right) u_j\left(\mathbf{x}\right) n_k\left(\mathbf{x}\right)\right] d\Gamma, \tag{3.23}$$

in which all the Green's functions J_{ij} and K_{ijk} are specified everywhere on Γ. In analogy to (3.23), the velocity in a point lying in the area S bounded by Γ, satisfies

$$u_i\left(\mathbf{x}_0\right) = \frac{1}{4\pi\mu} \oint_\Gamma \left[J_{ij}\left(\mathbf{x} - \mathbf{x}_0\right) f_j\left(\mathbf{x}\right) - K_{ijk}\left(\mathbf{x} - \mathbf{x}_0\right) u_j\left(\mathbf{x}\right) n_k\left(\mathbf{x}\right)\right] d\Gamma, \tag{3.24}$$

which implies that for any point $\mathbf{x}_0$, the velocity and traction are related by a single equation, which reads

$$c_{ij}\left(\mathbf{x}_0\right) u_j\left(\mathbf{x}_0\right) = \frac{1}{4\pi\mu} \oint_\Gamma \left[J_{ij}\left(\mathbf{x} - \mathbf{x}_0\right) f_j\left(\mathbf{x}\right) - K_{ijk}\left(\mathbf{x} - \mathbf{x}_0\right) u_j\left(\mathbf{x}\right) n_k\left(\mathbf{x}\right)\right] d\Gamma, \tag{3.25}$$

in which c_{ij} is defined as

$$c_{ij}\left(\mathbf{x}_0\right) = \begin{cases} \delta_{ij} & \text{if } x \in S \\ \frac{1}{2}\delta_{ij} & \text{if } x \in \Gamma \\ 0 & \text{otherwise} \end{cases} \tag{3.26}$$

It follows from equation (3.23) that if either the traction or the velocity is known on the boundary, the unknown quantity can be found. Since the traction depends on the gradients of the velocity components, the following two types of integral equations can be distinguished: if the velocity is given

on the entire boundary, equation (3.23) is a Fredholm equation of the first kind, whereas a specified traction leads to a Fredholm equation of the second kind. The latter does not have a unique solution, which means that there are multiple velocity fields corresponding to the same traction. This corresponds however to the physical problem, in which any constant velocity can be added to the field without changing the stress tensor and thus the traction, since the stress tensor only depends on velocity gradients.

3.2.1 Regularization of the integral equation

The integrals can be evaluated numerically and, under certain conditions, analytically. These conditions mainly involve the boundary of the domain, which must be free of singularities and discontinuities. Recalling the two-dimensional Green's functions, it can directly be seen that J_{ij} contains a logarithmic singularity for $\mathbf{x} = \mathbf{x}_0$, whereas K_{ijk} contains a stronger r^{-1} singularity. The logarithmic singularity is weak, i.e. diverging slower than r^{-1}, and can be removed by a coordinate transformation. The r^{-1} singularity in the K_{ijk} integral however can not be removed by such a transformation, implying a different method is needed. A simple but effective way to remove both singularities in the same way, is to subsequently subtract and add the appropriate products in the singular points to the integrand, thus converting (3.23) to

$$\begin{aligned} c_{ij}\left(\mathbf{x}_0\right) u_j\left(\mathbf{x}_0\right) &= \frac{1}{4\pi\mu} \oint_\Gamma J_{ij}\left(\mathbf{x}-\mathbf{x}_0\right) \left[\sigma_{jk}\left(\mathbf{x}\right) - \sigma_{jk}\left(\mathbf{x}_0\right)\right] n_k\left(\mathbf{x}\right) d\Gamma \\ &+ \frac{1}{4\pi\mu} \oint_\Gamma J_{ij}\left(\mathbf{x}-\mathbf{x}_0\right) \sigma_{jk}\left(\mathbf{x}_0\right) n_k\left(\mathbf{x}\right) d\Gamma \\ &- \frac{1}{4\pi\mu} \oint_\Gamma K_{ijk}\left(\mathbf{x}-\mathbf{x}_0\right) \left[u_j\left(\mathbf{x}\right) - u_j\left(\mathbf{x}_0\right)\right] n_k\left(\mathbf{x}\right) d\Gamma \\ &- \frac{1}{4\pi\mu} \oint_\Gamma K_{ijk}\left(\mathbf{x}-\mathbf{x}_0\right) u_j\left(\mathbf{x}_0\right) n_k\left(\mathbf{x}\right) d\Gamma. \end{aligned} \tag{3.27}$$

It can however immediately be seen that the integrand of the first integral can not be rewritten back into a traction form, since the product $\sigma_{jk}\left(\mathbf{x}_0\right) n_k\left(\mathbf{x}\right)$ does not satisfy (3.22) for all $\mathbf{x} \in \Gamma$. This implies that all components of $\sigma_{jk}\left(\mathbf{x}_0\right)$ remain in the integral and that the equations would contain twice as many unknowns as there are equations, since the stress tensor has four components instead of the two traction components. Therefore, the logarithmic singularity in the J-kernel can not be removed similar to the K-singularity and will therefore be removed using a coordinate transformation.

In the K integral, the singularities in the kernels are now removed by the term $u_j\left(\mathbf{x}\right) - u_j\left(\mathbf{x}_0\right)$. The additional terms can be simplified using the

definition of the Green's functions as solutions to the singularly forced Stokes flow. For the K integral, it follows that

$$\begin{aligned}
\oint_\Gamma K_{ijk}\left(\mathbf{x}-\mathbf{x}_0\right) u_j\left(\mathbf{x}_0\right) n_k\left(\mathbf{x}\right) d\Gamma &= u_j\left(\mathbf{x}_0\right) \oint_\Gamma K_{ijk}\left(\mathbf{x}-\mathbf{x}_0\right) n_k\left(\mathbf{x}\right) d\Gamma \\
&= u_j\left(\mathbf{x}_0\right) \oint_\Gamma \frac{\partial}{\partial x_k} K_{ijk}\left(\mathbf{x}-\mathbf{x}_0\right) d\Gamma \\
&= u_j\left(\mathbf{x}_0\right) \oint_\Gamma -4\mu\pi\delta_{ij}\delta\left(\mathbf{x}-\mathbf{x}_0\right) d\Gamma \\
&= -4\mu\pi c_{ij}\left(\mathbf{x}_0\right) u_j\left(\mathbf{x}_0\right), \qquad (3.28)
\end{aligned}$$

The boundary integral equation is now free of singularities and reads

$$c_{ij}\left(\mathbf{x}_0\right) u_j\left(\mathbf{x}_0\right) = \frac{1}{4\pi\mu} \oint_\Gamma J_{ij}\left(\mathbf{x}-\mathbf{x}_0\right) f_j\left(\mathbf{x}\right) d\Gamma \qquad (3.29)$$

$$-\frac{1}{4\pi\mu} \oint_\Gamma K_{ijk}\left(\mathbf{x}-\mathbf{x}_0\right) \left[u_j\left(\mathbf{x}\right) - u_j\left(\mathbf{x}_0\right)\right] n_k\left(\mathbf{x}\right) d\Gamma + c_{ij}\left(\mathbf{x}_0\right) u_j\left(\mathbf{x}_0\right),$$

from which it can be immediately seen that the velocity terms outside the integrals cancel. The final regular integral equation then can be written as

$$\oint_\Gamma J_{ij}\left(\mathbf{x}-\mathbf{x}_0\right) f_j\left(\mathbf{x}\right) d\Gamma = \oint_\Gamma K_{ijk}\left(\mathbf{x}-\mathbf{x}_0\right) \left[u_j\left(\mathbf{x}\right) - u_j\left(\mathbf{x}_0\right)\right] n_k\left(\mathbf{x}\right) d\Gamma. \qquad (3.30)$$

This equation is free of singularities and can thus be used to calculate the traction and/or velocity of the boundary. It will serves as the basis for the numerical calculations performed by the new code.

Chapter 4

Numerical methods

In this chapter, the numerical code used for the calculations will be discussed. The general scheme will be presented in section 4.1, whereas the remaining sections will focus on some essential components of the code; the geometry discretization will be presented in the second section, the numerical integration of the Green's functions will be discussed in section 4.3 and the final section is devoted to the solution algorithm.

4.1 General scheme

In this section, the general setup of the code will be presented. The basic features of the input/output processing, geometry initialization and updating will be presented, leaving the details of the discretization of the geometry for the next section. For convenience, the code is shown schematically in figure 4.1.

The input parameters are obtained from a manually prepared input file, which contains several essential parameters specifying the dimensions of the boundary, the asperity dimensions, lubricant viscosity and several discretization and interpolation parameters. Subsequently, the boundary and, if desired, domain collocation points are defined such that the discretized boundary satisfies the conditions following from the input specifications. In the discretization of both the boundary and the domain, the positions of the collocation points are defined such that integration over corners (in the discretization of the boundary) or over parts of the boundary (in the discretization of the domain) is prevented. In addition to this, the boundary quantities, i.e. velocity and traction, are set to the specified values as given by the input parameters, so that there is a discretized domain with identically discretized boundary conditions. The discretization will be discussed in more detail in the next section.

Following the initialization step, the actual calculations start. In every time step, the unknown velocities and tractions are calculated from the

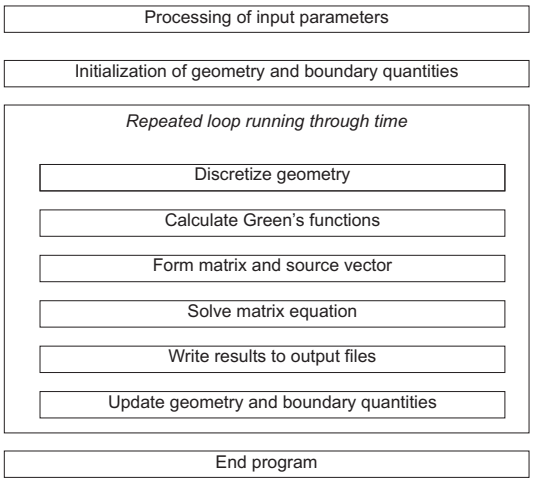

Figure 4.1: Calculation scheme of the code.

specified boundary quantities. These calculations require an additional discretization routine, in which the boundary is divided into intervals of which the collocation points are the center. Furthermore, the normals to these newly formed intervals as well as their individual lengths are computed. The boundary is now converted to a piecewise continuous, discrete form, which can be used for the integration of the Green's functions.

Using the discretized boundary properties, the Green's functions J_{ik} and K_{ijk} can be calculated and integrated for every couple of collocation points. In the case of N collocation points and a two-dimensional system, these calculations result into eight N x N matrices, four for each of the two Green's functions. The dot product of the appropriate matrix elements with the specified boundary quantities leads to the formation of the right hand side vector of the matrix equation.

The thus obtained matrix equation is solved using a numerical solution algorithm, resulting into a vector containing all the unknown boundary quantities. Iteration criteria for the solver and the actual solving algorithm will be discussed later on. Finally, the time and the positions of the collocation points are updated so that the velocities and tractions can be recomputed for the next time step.

4.2 Discretization of boundary and time-stepping algorithm

In this section, the discretization of the boundary will be discussed in more detail. The discretization principles presented in section 4.1 will serve as

the basis for the discussion. Special attention will be paid to the available options regarding the intervals and boundary conditions. Finally, the time progress will be briefly explained.

As stated in the previous section, the boundary is discretized by dividing the integration paths Γ_I to Γ_{IV} into N elements Γ_n of finite length. Since the length of $\Gamma_{I,III}$ can be chosen to be different from the length of $\Gamma_{II,IV}$, the horizontal and vertical boundaries will be discretized separately into N_L and N_H elements respectively, leading to a total number of elements $N = 2\,(N_L + N_H)$. A sketch of the discretization is shown in figure 4.2, in which the italic numbers represent the begin and endpoints of the elements and the non-italic numbers represent the collocation points of the elements, which will be introduced later. The end point of the N^{th} element is equal

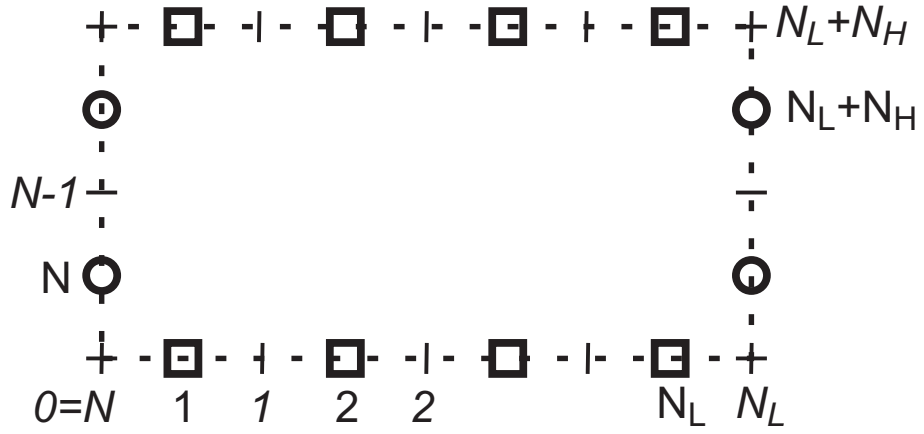

Figure 4.2: Discretization of the boundary into N finite elements.

to the begin point of the first interval, thus forming a closed contour. The distinction between boundary intervals with specified velocity and specified traction is preserved by positioning element begin and end points in the corners, so that on each element, either the velocity or the traction is known. A beneficial side effect of this discretization choice is that all the boundary corners are positioned at the beginning or end of an element, thus avoiding possible discontinuities in the integration paths.

The intervals can be approximated in numerous ways. The most straightforward approximation is the linear representation, which is also the one shown in figure 4.2. However, some sources [8] suggest the use of circular arcs or cubic splines. Obviously, these more complicated approximations improve the accuracy of the boundary discretization in the case of complex, non-linearly shaped geometries, although this is at the cost of computational speed. In addition to the increased calculation times, complications at the corners of the boundary will occur, since more accurate approximations use a

larger number of collocation points to determine the shape of the calculated interval, which will cause problems if one of the boundary corners is within this number of points. This implies that for intervals close to the boundary corners, the approximation interval will contain a discontinuity, which will clearly affect the accuracy. As the boundary initially consists of straight lines and Couette or strongly Couette-like velocity profiles are anticipated, the linear approximation will be chosen to discretize the boundary. The relatively low number of calculations needed for the approximation confirms this choice.

A similar dilemma between computation speed and accuracy occurs at the discretization of the boundary conditions. The simplest method is to assume constant quantities over the entire interval, irrespective of the values of similar quantities on the neighboring intervals. The velocity and/or traction of the interval are then considered equal to the velocity and/or traction in the corresponding collocation point. Again, some sources [14], [15] suggest the use of higher order approximations, based on the quantities in neighboring collocation points. However, for similar reasons as above, the simplest method is chosen since it is easier to implement and segment calculation over boundary corners is avoided.

The updating of time and geometry can be done in various ways, such as a variable time step [16], which is calculated from the boundary velocity. In order to avoid these additional calculations, the time step is kept at a constant value, which is obtained from the input file. The boundary is updated by adjusting the positions of each collocation point $\mathbf{x}_m$ using the straightforward expression

$$\mathbf{x}_m\left(t+\Delta t\right)=\mathbf{x}\left(t\right)+\mathbf{u}\left(\mathbf{x}_m,t\right)\Delta t, \tag{4.1}$$

in which Δt represents the fixed time step. The intervals and their normals and lengths are updated when they are recalculated at the beginning of the next time step, since these calculations are fully based on the positions of the collocation points.

4.3 Calculation of the matrix and the source vector components

This section contains the details of the matrix and right hand side vector elements calculation. In order to obtain the appropriate matrix and vector, three steps are taken: first of all, the Green's functions are calculated and integrated, then the calculated elements are stored in the matrix and finally, the dot products of the specified boundary quantities with the corresponding matrix elements are taken to form the source vector. Regarding the Green's functions, special attention has to be paid to the treatment of singularities in these functions.

The matrices relating boundary velocities to boundary tractions are composed of Green's functions integrated over a certain part of the boundary. More specifically, the m, n-components of the matrices are given by

$$A_{ij}^{mn} = \int_{\Gamma_n} J_{ij}\left(\mathbf{x}, \mathbf{x}_m\right) d\Gamma \tag{4.2}$$

and

$$B_{ij}^{mn} = \int_{\Gamma_n} K_{ijk}\left(\mathbf{x}, \mathbf{x}_m\right) n_k\left(\mathbf{x}\right) d\Gamma \tag{4.3}$$

in which Γ_n is a straight line segment around $\mathbf{x}_n$ and J_{ij} and K_{ijk} are the Green's functions given by (3.12) and (3.16). Following Toose [16], the integrals will be solved using Gaussian quadrature methods and the A and B elements are arranged such that the regularized integral equation (3.30) is satisfied. The regularized integral equation is then converted to a matrix equation that reads

$$A_{ij}^{mn} f_j^n = B_{ij}^{mn} \left[u_j^n - u_j^m\right]. \tag{4.4}$$

In accordance with section 3.2, in which it was stated that any constant velocity can be added to the velocity field without influencing the traction, it is noted in (4.4) that from a fully specified traction, only velocity differences can be calculated. By rearranging the terms on the right-hand side, equation (4.4) can be rewritten into a simplified form,

$$A_{ij}^{mn} f_j^n = \tilde{B}_{ij}^{mn} u_j^n. \tag{4.5}$$

The unknown and specified quantities can now be brought to different sides of the equation. For the unknowns, this leads to a vector v_n, containing all the unknown quantities, and a matrix M consisting of the A and B components corresponding to components of v_n. For the specified quantities, the matrix products can be computed and stored in a right-hand side vector b_m, which is also referred to as the source vector. The final form of the matrix equation then reads

$$M^{mn} v^n = b^m, \tag{4.6}$$

which can be solved using standard matrix equation solution algorithms.

The accuracy of the A and B components depends on two contributions: the interval length and the order of the Gaussian quadrature. Since a smaller interval length and a higher quadrature order decrease the error, it is anticipated that both increasing the number of collocation points and quadrature order will lead to higher accuracy if the singularities are properly dealt with. In order to verify this hypothesis, the integrals have been calculated for several different numbers of collocation points and quadrature orders and compared to their analytically calculated counterparts, which

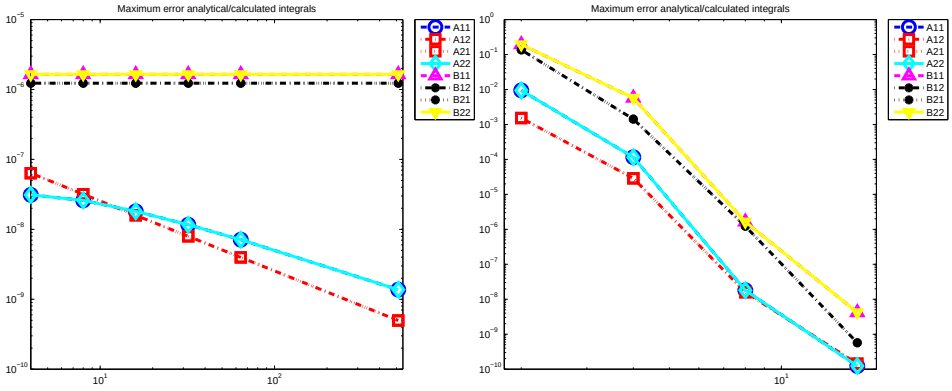

(a) Variable number of collocation points. (b) Variable quadrature order.

Figure 4.3: Maximum absolute error of integrals calculated using Gaussian quadrature.

have been integrated along the same straight segments using the antiderivatives of the Green's functions. The left figure displays the maximum error in the A and B matrices as a function of the number of collocation points, with a constant quadrature order of eight. The maximum error of a matrix is defined by

$$E_{A_{ij}} = \max_{mn} \left| A_{ij}^{mn,numerical} - A_{ij}^{mn,analytical} \right|. \tag{4.7}$$

In the right figure, the error is computed similarly for a variety of quadrature orders, with a constant number of 16 collocation points. Figure 4.3a shows that increasing the number of collocation points is only beneficial for the accuracy of the A components, whereas the B components have a constant error of the order of 10^{-6}. As can be seen in figure 4.3b, the quadrature order influences the accuracies of all matrix components.

Assuming the maximum error corresponds to the integrals over interval nearest to a singulary, this is in correspondence with the expected behavior derived from the definition of the quadrature approximation: for a given number of collocation points N, the interval length is $\frac{2L}{N}$. Then, for a given quadrature order G, the B component consisting of the integral over the interval nearest to the interval containing the singularity is approximated by

$$\int_{\frac{L}{N}}^{\frac{3L}{N}} \frac{dr}{r} \approx \frac{L}{N} \sum_{i=1}^{G} w_i \frac{1}{\frac{L}{N} x_i + \frac{L}{N}} = \sum_{i=1}^{G} w_i \frac{1}{x_i + 1}, \tag{4.8}$$

in which w_i and x_i are the Gaussian quadrature weights and points, respectively. Expression 4.8 proves that the accuracy of the numerically evaluated

K-integral only depends on the quadrature order; it is independent of the interval length.

For the A components, a similar derivation leads to

$$\int_{\frac{L}{N}}^{\frac{3L}{N}} \ln r dr \approx \frac{L}{N} \sum_{i=1}^{G} w_i \ln \left(\frac{L}{N} x_i + \frac{L}{N} \right) = \frac{L}{N} \left(\ln \frac{L}{N} + \sum_{i=1}^{G} w_i \ln \left(x_i + 1 \right) \right), \tag{4.9}$$

which shows an accuracy dependence on both N and G. Thus, the accuracy of the A components increases with both increasing number of collocation points and quadrature order, whereas the accuracy of the B components increases with increasing quadrature order, but is independent on the number of collocation points. This is confirmed by the results shown in figure 4.3a, in which it can be seen that the maximum absolute error decreases with increasing N for the A components, whereas the error in the B components is constant for all N. On the other hand, figure 4.3b shows that both the A and B components are calculated more accurately as the quadrature order increases.

For an eighth order quadrature, the error is again of the order of 10^{-6}. The fourth order quadrature, which is computationally less costly, has a maximum error of the order of 10^{-2}, which is approximately 1 to 10 percent of the matrix components magnitude. Therefore, eighth order quadrature will be used henceforth.

Considering the positioning of the A- and B-elements in the final matrix M, there are several possibilities, of which two will be briefly discussed here. The first possibility is to compose a matrix of all integrated Green's functions and form a corresponding work array of all boundary quantities. The specified quantities and their corresponding matrix rows and columns can then be eliminated from both the matrix and the work array and are stored in the right hand side vector. A major drawback of this approach is that it is rather elaborate to implement, since the matrix and source vector have to be refilled after every elimination step. Moreover, the initial matrix consists of four times as many elements as the final one, which makes this approach computationally costly, regarding both memory and calculation time.

A faster way is to introduce so-called flavors: variables indicating whether in a certain collocation point, the velocity is unknown and the traction is specified, or the other way round. The work array is then directly formed of all the unknowns and the matrix is subsequently formed based on the work array: the flavor of the j^{th} collocation point determines whether the j^{th} element of the work array is the traction or the velocity and that determines whether the j^{th} column of the matrix consists of A-elements or B-elements, respectively. This method is more prone to programming errors and incorrect flavor allocation, but produces the matrix and vector at the desired dimensions immediately and guarantees the appropriate calculation of the

dot products that form the right hand side vector.

4.4 Solution algorithm

The matrix equation that is obtained from the integrated Green's functions and the boundary conditions, needs to be solved in order to find the values of the unknown quantities. Among the wide variety of solvers for matrix equations or linear sets of equations, a few are discussed in this section.

Among the most stable methods are elimination algorithms such as Gaussian elimination and Gauss-Jordan elimination. These methods however require an enormous number of calculations for larger number of collocation points, since the number of calculations roughly scales with the number of equations to the third power. Considering the large number of collocation points that may be desired if complex geometries are modeled, the use of elimination methods is not desirable.

The most common alternative to elimination is iteration. Iterative methods calculate approximations of the solution of a matrix equation using the previous approximation, starting from an initial approximation that is mostly obtained from the solution in the previous time step. If the method is successful, the approximations will converge towards the correct solution, implying that the iteration can be stopped when the difference between two consecutive approximations is smaller than a pre-defined criterion. One of the simplest iterative methods is the Jacobi algorithm, which guarantees convergence for any strictly diagonally dominant matrix, i.e. a matrix for which

$$|M_{ii}| > \sum_{i \neq j} |M_{ij}| \tag{4.10}$$

holds for every row i. Convergence is also guaranteed for irreducibly diagonal dominant matrices, for which is satisfied for at least one row and the other rows satisfy the weaker requirement

$$|M_{ii}| \geq \sum_{i \neq j} |M_{ij}| \,. \tag{4.11}$$

Test calculations have shown that if neither of these requirements is satisfied, convergence can still be reached in some cases when the diagonal elements are in absolute value larger than all the other elements of that row individually. A major drawback of the Jacobi method however is that it uses all components of the previous iterand, thus requiring double storage memory. This problem is overcome in the Gauss-Seidel method, which allows overwriting of approximation arrays. However, the strict convergence requirements of the Jacobi method apply to the Gauss-Seidel algorithm as well.

The use of the Cauchy principal value integral for the K-integral implies that the matrix will not be diagonally dominant if at least one velocity is unknown. This is a consequence of the fact that the diagonal elements of the B matrices contain the r^{-1} singularity and are therefore removed by the principal value method, which replaces them with the sum over all other elements of the row. This implies that the absolute value of the diagonal element is equal to the sum of the absolute values of the other elements of the row if all row elements have the same sign. If at least two elements have opposite sign, the sum of absolute values will be larger than the absolute diagonal element and (4.4) is no longer satisfied. The influence of the J-integral on the diagonal dominance of the matrix strongly depends on the number of collocation points, since the result of the integral over the logarithmic singularity largely depends on the length of the integration interval. Thus, diagonal dominance can be guaranteed by neither a matrix consisting solely of A elements, nor a similar matrix with exclusively B elements and it is therefore unlikely that a matrix containing both A and B components will be diagonally dominant for all geometries. However, the weakest requirement,

$$|M_{ii}| > |M_{ij}| \forall j \neq i, \tag{4.12}$$

is easily satisfied and in practice, the Gauss-Seidel method converges, albeit sometimes slowly, to an appropriate solution and can therefore be used without much risk.

Mathematically, the Gauss-Seidel method computes the k^{th} iteration of the i^{th} vector component, represented by v_i^k, using

$$v_i^k = \frac{1}{M_{ii}} \left(b_i - \sum_{j<i} M_{ij} v_j^k - \sum_{j>i} M_{ij} v_j^{k-1} \right). \tag{4.13}$$

From this expression [17], it can be seen that the Gauss-Seidel method continuously overwrites the solution array, thus keeping the memory usage to a minimum.

The convergence criterion is based on the L2-norm of the difference vector of two consecutive iterands, implying that at each step k, the following residual is calculated and compared to a reference value of, for instance, 10^{-6}:

$$R^k = \frac{1}{N} \sqrt{\sum_{i=1}^{N} \left(u_i^k - u_i^{k-1} \right)^2}. \tag{4.14}$$

An additional criterion is defined to prevent the algorithm from getting into an infinite loop in case the solution does not converge and is simply based on a maximum number of iteration steps the solver is allowed to reach a stable and converged solution.

Chapter 5

Validation of the code

In this chapter, the validation of the code and the results from calculations are presented. In the first section, the validation test is introduced and the outcome is discussed. The second and third sections of the chapter are devoted to calculations on a series of similar problems, for which no analytical solutions are known. These problems are based on the validation test, with an asperity of variable dimensions added to the geometry. Finally, in section 5.4, a brief discussion on the geometrical limitations of the code is given.

5.1 Flow between two parallel flat walls

The simplest test case to be modeled is the flow between two parallel flat walls, since the well-known solution for infinitely long walls, Couette flow, provides a linear velocity profile and, as a consequence, a constant traction along each wall. For walls of finite length, the velocity field is identical to the Couette field under the appropriate boundary conditions; on the vertical boundaries that are absent in the case of infinitely long walls, either a specified velocity profile or a stress profile has to be specified such that it corresponds to Couette flow. This implies that if the velocity is specified on the vertical boundaries, it has to satisfy a linear profile for the horizontal component, whereas the vertical component has to equal zero on the entire vertical boundary. On the other hand, if the traction is specified, it has to be derived from the aforementioned velocity profile and a constant pressure in the entire domain, yielding the product of the constant stress tensor of expression (2.25) and the constant normal at the vertical boundary, and thus a constant traction profile.

If the boundary conditions are defined as discussed above, the horizontal velocity is independent of x_1 as a consequence of the x_1-independence of the vertical cross-section of the domain. From the continuity equation (**??**) and the no-slip condition at the top and bottom walls, it follows that the vertical

velocity is zero anywhere in the domain. Invoking the Stokes equations, the pressure inside the domain can only be x_1-dependent, which is different from Couette flow, in which the pressure is constant.

The boundary conditions for the problem arise directly from the motion of the walls and the desire to calculate the velocity profiles between the walls: on the two walls, the velocity is specified and on the two vertical boundary parts, the traction has to be specified to enable calculation of the velocity on these boundary parts. As mentioned before, the traction has to be defined such that it satisfies Couette's solution, leading to

$$\begin{aligned} f_1 &= \sigma_{11} n_1 + \sigma_{12} n_2 \\ &= \left(-p + 2\mu \partial_1 u_1\right) n_1 + \mu \left(\partial_2 u_1 + \partial_1 u_2\right) n_2 \\ &= -p n_1 + \mu \partial_2 u_1 n_2 \end{aligned} \tag{5.1}$$

and for the vertical traction, it yields

$$\begin{aligned} f_2 &= \sigma_{21} n_1 + \sigma_{22} n_2 \\ &= \mu \left(\partial_2 u_1 + \partial_1 u_2\right) n_1 + \left(-p + 2\mu \partial_2 u_2\right) n_2 \\ &= \mu \partial_2 u_1 n_1 - p n_2, \end{aligned} \tag{5.2}$$

On the vertical boundaries, the normal vector is purely horizontal, implying that the pressure can only influence the horizontal traction on these boundaries. As the pressure consists of the atmospheric pressure and a hydrodynamic contribution and only its gradient is used in the Stokes equations (2.10), this constant can be any value and is set to zero for convenience. The other contribution to the traction, the velocity gradient, can be computed by taking the derivative of the Couette profile (2.24),

$$\partial_2 u_1 = \partial_2 \left(\frac{U}{H} x_2 \right) = \frac{U}{H}. \tag{5.3}$$

For reasons of simplicity, a domain of unit height and length is chosen and the viscosity of the fluid is also set to 1. By choosing the specified horizontal velocity of the bottom and top wall to be -1 and $+1$ respectively, the full set of boundary conditions can be calculated and is given by

$$x_2 = -1 \quad : \quad u_1 = -1, u_2 = 0; \tag{5.4}$$

$$x_1 = 1 \quad : \quad f_1 = 0, f_2 = -1; \tag{5.5}$$

$$x_2 = 1 \quad : \quad u_1 = 1, u_2 = 0; \tag{5.6}$$

$$x_2 = -1 \quad : \quad f_1 = 0, f_2 = 1. \tag{5.7}$$

For convenience, the domain and the boundary conditions are displayed in figure 5.1. A major consequence of the finite wall length is the presence of corners in the boundary, which belong to the two adjacent boundary

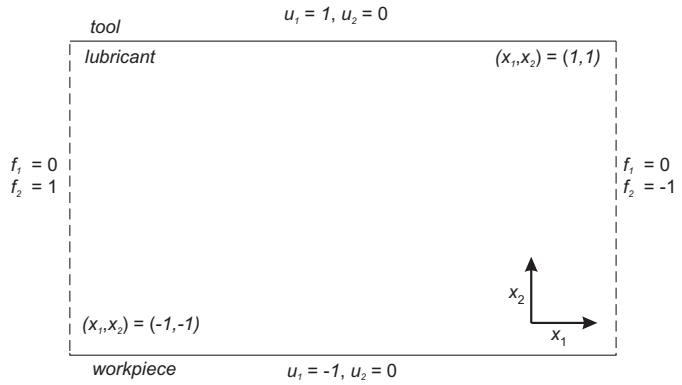

Figure 5.1: Validation domain with boundary conditions.

intervals with different boundary conditions. Moreover, the normal vectors of the adjacent boundary intervals are perpendicular, implying that the normal, and thereby the traction, will be ill-defined at the corner. As a consequence, the solutions for the traction and the velocity may deviate from the expected profiles near the corners of the boundary.

5.1.1 Results of the validation

For several numbers of collocation points, ranging from 1 point per part of the boundary to 64 points per part of the boundary, i.e. 4 to 256 points in total, the velocities at the vertical boundaries as well as the tractions at the horizontal boundaries have been calculated. As stated at the beginning of this section, it is anticipated that the horizontal velocity shows a linear dependence on the vertical coordinate, whereas the vertical velocity is zero on the entire boundary. The horizontal traction on the horizontal wall, which has a purely vertical normal vector, is expected to equal the constant velocity gradient, which is equal to 1. The vertical traction is equal to the pressure and will thus depend on x_1.

Figures 5.2a and 5.2b show the velocity profiles on the right vertical boundary, given by $x_1 = 1$. In figure 5.2a, it can be seen that, apart from $N = 8$, the calculated velocities satisfy the expected Couette profile very well. Figure 5.2b shows that for increasing number of collocation points, the calculated solutions converge to the expected Couette solution. In fact, both the differences between the calculated and the expected solutions and the intervals near the corners for which the velocity is calculated inaccurately decrease rapidly with increasing number of collocation points.

Similar figures can be made for the calculated and expected traction, as can be seen in figures 5.3a and 5.3b. For the horizontal traction, a similar observation can be made as for the vertical velocity: for increasing numbers

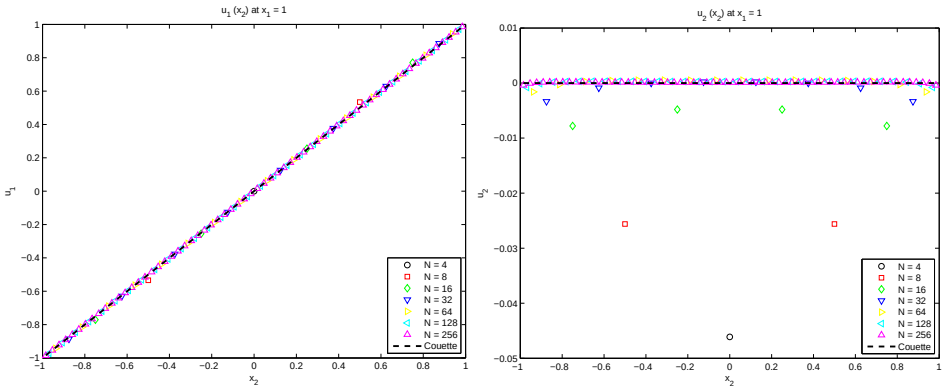

(a) Horizontal velocity. (b) Vertical velocity.

Figure 5.2: Velocity profiles on the right vertical boundary.

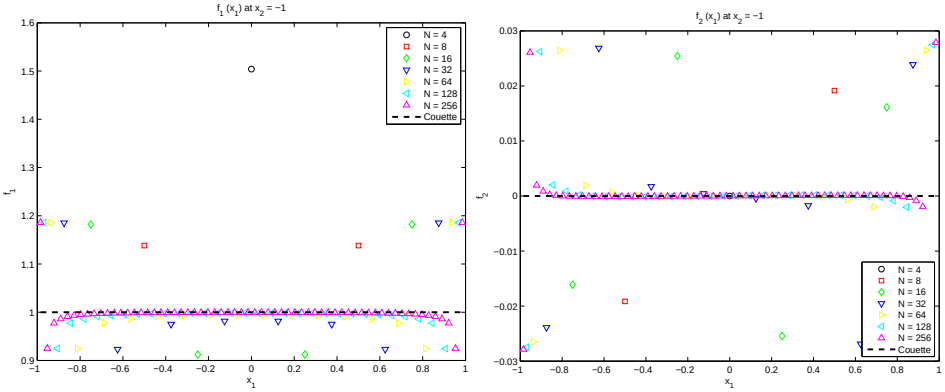

(a) Horizontal traction. (b) Vertical traction.

Figure 5.3: Traction profiles on the bottom horizontal boundary.

of collocation points, both the overall inaccuracy and the interval of deviations near the corners decrease. In fact, it can be seen in figure 5.3a that these intervals merely cover a constant number of collocation points instead of a constant part of the boundary. However, the calculated traction values at the corners tend to increase slightly (horizontal traction) or more rapidly (vertical traction) with increasing number of collocation points. This indicates singular behavior near the corners, which can be attributed to the normal vector that is not defined at the corners, as discussed in the previous section.

5.1.2 Convergence speed

In the previous subsection, it has been established that a larger number of collocation points increases the accuracy of the solution. However, it increases the number of computations and thereby the overall calculation time. This time increase can be compensated, fully or partially, if the iterative solver reaches a converged solution after a smaller number of iterations. The number of iterations needed to reach a converged solution, as defined in section 4.4 is displayed as a function of the number of collocation points in figure 5.4. From figure 5.4, it can be concluded that increasing the number of

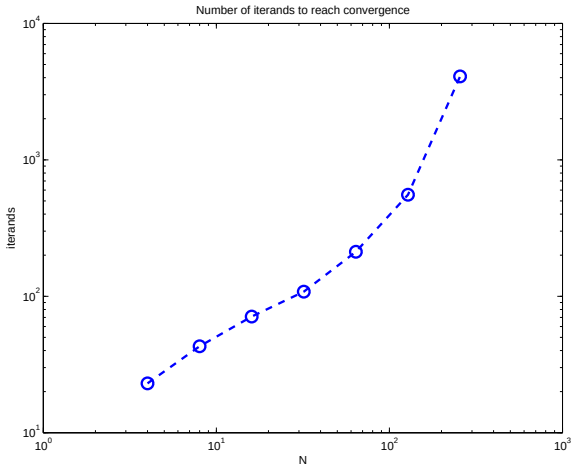

Figure 5.4: Convergence speed as a function of the number of points.

collocation points leads to a significant increase in the number of iterations needed to reach a converged solution. This implies that a larger number of collocation points has a beneficial effect on the accuracy of the solution, but a negative effect on the calculation time.

5.2 Influence of the number of collocation points on the flow between a flat and a rough wall

The flow between a flat top wall and a bottom wall with a single asperity of height $\epsilon = \frac{1}{2}$ and width $\delta = \frac{1}{4}$, positioned at the center of the wall, is considered. In this section, the influence of the number of collocation points on the calculated solution for the boundary velocity is discussed, as well as the influence on the velocity in the domain. It is anticipated that for an increasing number of collocation points, the calculated solution will converge to a series of values representing the solution that would be found in the limit of infinite numerical accuracy.

A sketch of the single asperity geometry is shown in figure 5.5. The red

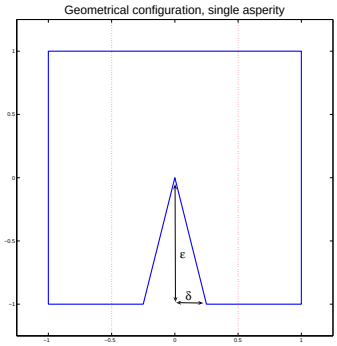

Figure 5.5: Sketch of the single asperity geometry.

lines in figure 5.5 indicate the maximum width of the asperity. This interval is chosen such that all asperity dimensions modeled within the single asperity geometry have the asperity significantly separated from the boundary; in the calculations discussed in this chapter, the maximum asperity half width was $\delta_{max} = \frac{1}{4}$.

5.2.1 Velocity at the boundary

For several numbers of collocation points, the boundary velocity has been calculated using Couette boundary conditions (cf. section 5.1). It should be noted that for the vertical boundaries, the Couette conditions for the traction do not apply due to the asperity on the bottom wall. However, since the distance between the center of the asperity is four times as large as the asperity width, the influence of the asperity on the boundary velocity profile is assumed to be small, which makes the Couette conditions a useful approximation for the exact boundary conditions, which are unknown. The profiles of the horizontal and vertical velocity on the right boundary ($x_1 = L$) are displayed in figures 5.6a and 5.6b. Figure 5.6b clearly shows the expected converging behavior: with increasing number of collocation points, the difference between the solutions decreases, which implies that a converged solution is found. The calculated solutions are approximations of this solution of which the accuracy increases with increasing number of collocation points.

In figure 5.6a, the converging behavior can not be seen as clearly as in figure 5.6b. However, inspecting a smaller x_2-interval yields a clear view on the convergence of the calculated solutions, as can be seen in figure 5.7. In analogy to the vertical velocity, the differences between the horizontal

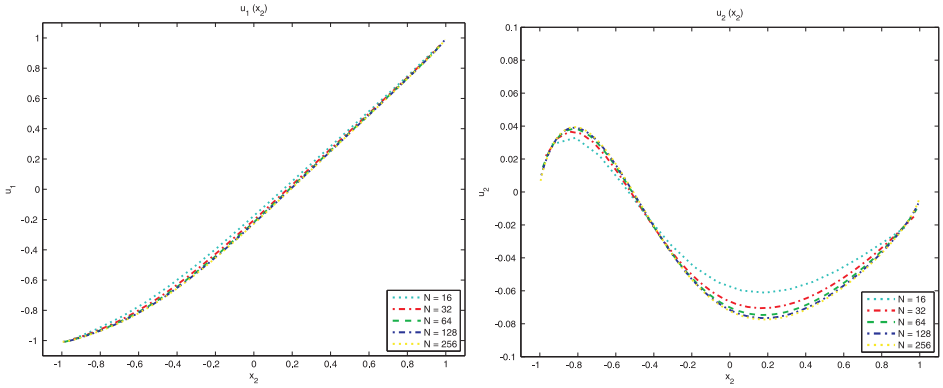

(a) Horizontal velocity. (b) Vertical velocity

Figure 5.6: Vertical profiles of the velocity components.

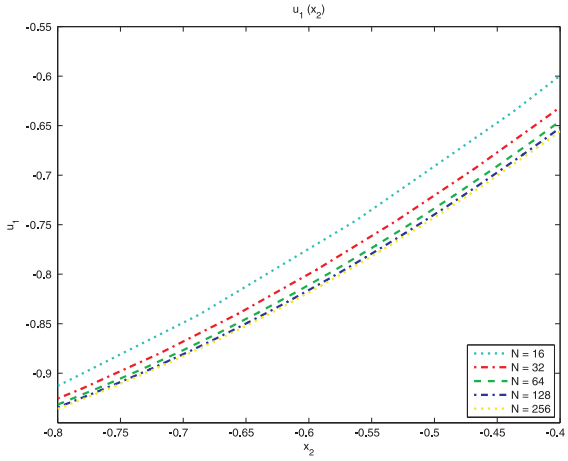

Figure 5.7: Horizontal velocity on a smaller interval.

velocity solutions decrease with increasing number of collocation points, thus leading to a converged solution for horizontal velocity profile.

5.2.2 Velocity in the domain

Using the boundary velocity profiles calculated in section 5.2.1, the velocity in the domain can be computed using (3.24). It is anticipated that the thus calculated velocity profiles will converge for increasing number of collocation points. A vertical cross-section is defined at the center of the asperity and it is discretized analogously to the vertical boundaries, implying that the

number of discretization points on the cross-section equals the number of collocation points per vertical boundary N_H. The horizontal and vertical velocity profiles are shown in figures 5.8a and 5.8b. In figure 5.8a, it can

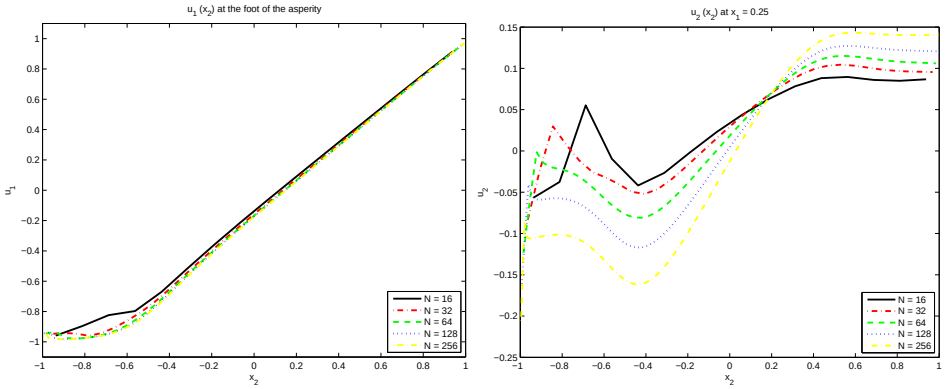

(a) Horizontal velocity.

(b) Vertical velocity

Figure 5.8: Vertical profiles of the velocity components at the asperity center.

be seen that the solution converge on the entire cross-section. In particular, converging behavior can clearly be observed close to the asperity top, where the discretization accuracy has the strongest N-dependence. Figure 5.8b does not display converging solutions, but all vertical velocities are of the order of 10^{-10}, which is negligibly small compared to the numerical accuracy of the integrated Green's functions, which is of the order of 10^{-6}. Thus, the solutions may be interpreted as $u_2 = 0$ for the entire cross-section, which is confirmed by the fact that the cross-section is positioned at the center of a symmetrical domain.

5.3 Influence of the asperity dimensions on the flow between a flat and a rough wall

In the previous section, it has been established that the solutions for the boundary velocity converge. As a consequence, the boundary solutions can be used to calculate similar vertical velocity profiles as well as pressure profiles anywhere in the domain bounded by the single asperity boundary of figure 5.5. In this section, the influence of the asperity dimensions on the velocity and pressure field is investigated. In the first subsection, asperities of constant area are studied, whereas the second subsection is devoted to asperities of constant width.

The influence of the asperity dimensions is studied using asperities of

constant area. This implies that for a given asperity height ϵ, the corresponding half-width δ_ϵ is given by

$$\delta_\epsilon = \frac{A_0}{\epsilon}, \tag{5.8}$$

in which A_0 represents the constant asperity area. Vertical profiles of the velocity components are computed from the boundary quantities at three points on the horizontal walls: $x_1 = 0$, corresponding to the center and top of the asperity, $x_1 = 0.25$, corresponding to the maximum asperity half-width and $x_1 = 0.9$, which is close to the right boundary and thereby relatively far from the asperity.

5.3.1 Influence on the velocity field

The horizontal and vertical profiles at the center of the horizontal walls are shown in figures 5.9a and 5.9b. From figure 5.9a, it can be seen that

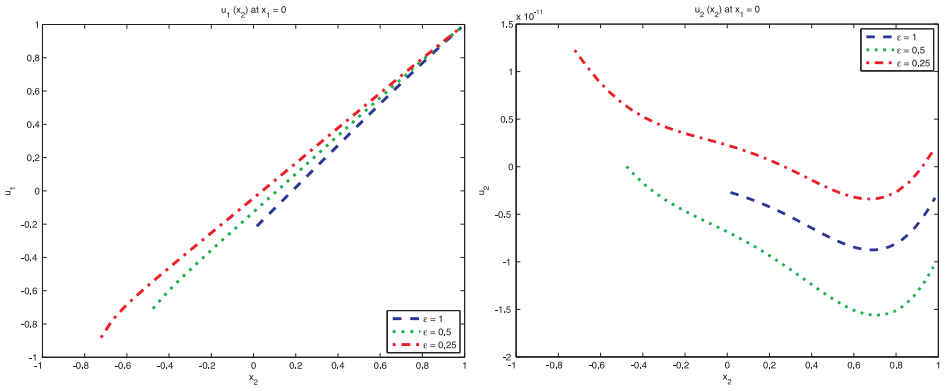

(a) Horizontal velocity. (b) Vertical velocity.

Figure 5.9: Velocity profiles at $x_1 = 0$.

the horizontal velocity gradient increases with increasing asperity height, an obvious consequence of the decreasing wall separation distance and the constant velocity difference between the two horizontal walls. However, the gradient increase is not large enough to ensure entirely linear velocity profiles, as the velocity profiles should range from the bottom wall velocity to the top wall velocity, which corresponds to the interval $-1 \leq u_1 \leq 1$. Figure 5.9a clearly shows that for increasing values of ϵ, the velocity difference between the bottom wall and a domain point just above the wall increases rapidly, which implies increasing gradients in the horizontal velocity close to the top of the asperity. Figure 5.9b shows that for all asperity heights considered, the vertical velocity has a maximum order of magnitude of 10^{-11},

which is below the numerical accuracy. It can thus be concluded that at $x_1 = 0$, the vertical velocity equals zero on the entire vertical profile, which is a consequence of the symmetry of the geometry.

For $x_1 = 0.25$, the velocity profiles are displayed in figures 5.10a and 5.10b. Figure 5.10a shows linear profiles far from the bottom wall, with

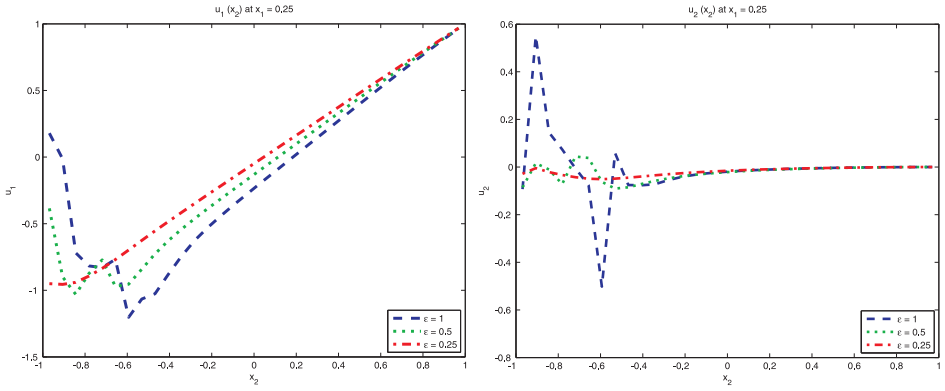

(a) Horizontal velocity. (b) Vertical velocity.

Figure 5.10: Velocity profiles at $x_1 = 0.25$.

non-linear behavior close to the bottom wall. Assuming that the non-linear behavior can be decomposed into the linear profile far from the wall and a non-linear contribution arising from flow disturbance by the asperity, it can be concluded that the disturbance increases with increasing asperity height. An analogous observation can be made in figure 5.10b, in which a height dependent disturbance is added to a constant profile corresponding to zero vertical velocity.

Finally, the velocity profiles for $x_1 = 0.9$ are shown in figures 5.11a and 5.11b. The horizontal velocity profiles show constant gradients for large x_2. Both the constant gradients and the x_2-intervals for which the profiles are non-linear increase with increasing ϵ. In addition, the vertical velocity shows an overall increase for increasing asperity heights.

Overall, the velocity profiles are smooth, except for $x_1 = 0.25$, which is close to the foot of the asperity. As a consequence of the triangular shape of the asperity, this implies the presence of a corner in the boundary where the normal vector is not defined, which influences the accuracy of the solution. The influence of the corners is also visible in the graphs of the velocity components in the entire domain, which are displayed in figures 5.12a and 5.12b, for $\epsilon = 0.25$. The graphs of figure 5.12a and 5.12b represent lines of constant velocity; this implies that velocity gradients increase when the lines converge and decrease when the lines diverge. The left figure clearly shows a local decrease in velocity near the corners on the bottom boundary, which

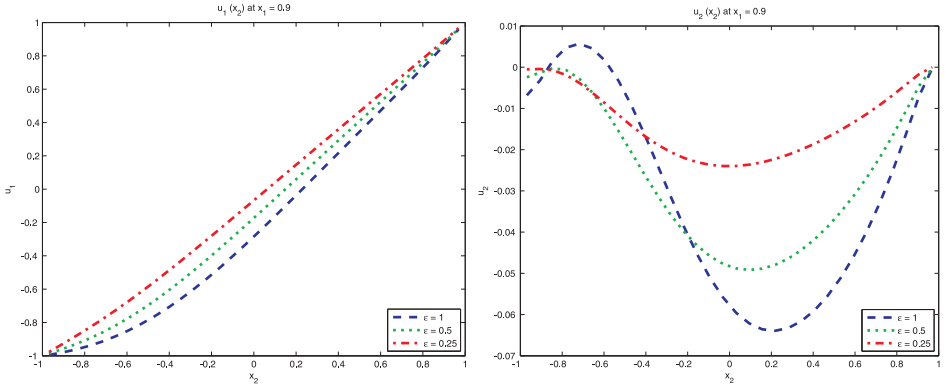

(a) Horizontal velocity. (b) Vertical velocity.

Figure 5.11: Velocity profiles at $x_1 = 0.9$.

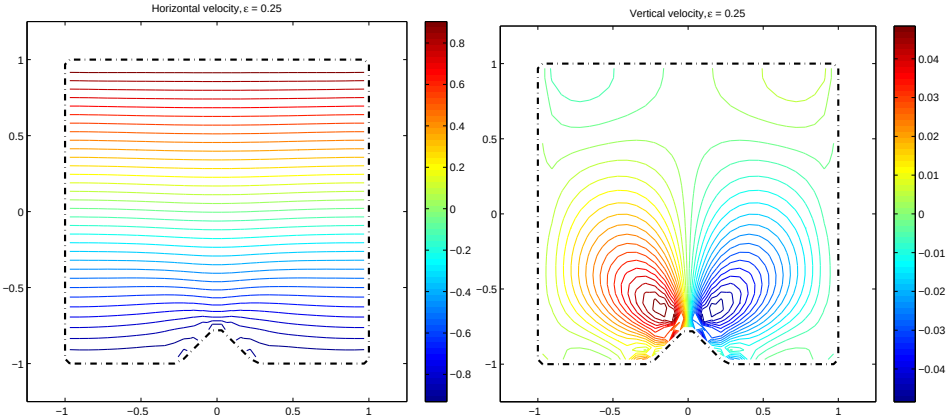

(a) Horizontal velocity. (b) Vertical velocity.

Figure 5.12: Domain plots of the horizontal and vertical velocity.

confirms the influence of the locally ill-defined boundary conditions. Similar observations can be made from figure 5.12b, in which large gradients can be seen near the asperity corners. For larger asperity height/width ratios, the corners are distributed over a smaller interval and the top corner of the asperity increases, thus increasing the disturbances to the flow field caused by the corners.

5.3.2 Influence on the maximum velocity and the friction

For asperities with a constant area, the influence of the asperity height on the geometry is twofold: increasing the height will decrease the separation between the two horizontal walls at the center of the asperity and the decreasing asperity width corresponding to an increasing height will cause a quadratic increase of the slope of the asperity. It is thus anticipated that increasing ϵ will lead to increasing absolute maxima for both the horizontal and the vertical velocity; the former as a consequence of the decreased separation, the latter as a consequence of the increased slope. The absolute maxima of the horizontal and vertical velocity as a function of the asperity height are shown in figures 5.13a and 5.13b. Figures 5.13a and 5.13b show

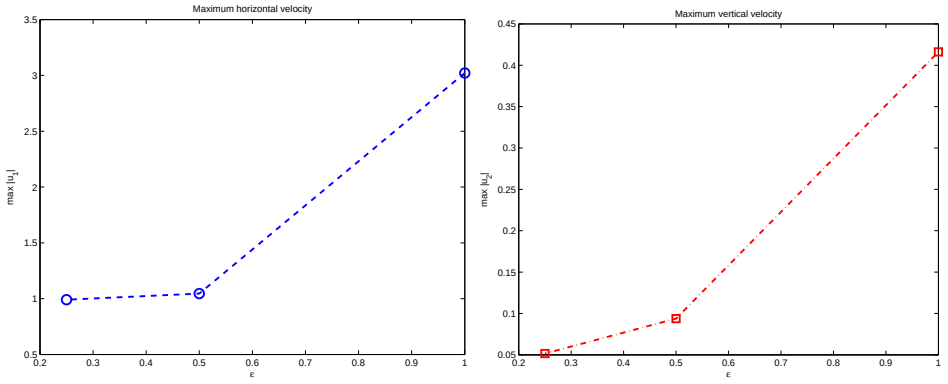

(a) Horizontal velocity. (b) Vertical velocity.

Figure 5.13: Absolute maxima of the velocity components.

the expected behavior: the absolute maxima of both velocity components increase with increasing asperity height. For $\epsilon = \frac{1}{2}$, the maximum absolute horizontal velocity even increases to three times the specified velocities of the top and bottom walls.

The hydrodynamic friction force at the top wall can be estimated from the velocity field:

$$F_w \equiv \int_A \sigma dA \approx \int_{-L}^{L} \mu \left(\partial_2 u_1\right)_{x_2=H} dx_1 \approx \sum_{n=1}^{N_L} \left(\partial_2 u_1\right)_H^n dx_1^n, \tag{5.9}$$

in which the velocity gradient is approximated by

$$\left(\partial_2 u_1\right)_H^n \approx \frac{U_1 - u_1^{N_H,n}}{H - x_2^{N_H,n}}, \tag{5.10}$$

with $u_1^{N_H,n}$ representing the horizontal velocity in the domain close to the top wall at $x_1 = x_1^n$. The estimated friction force is shown as a function of the

asperity height in figure 5.3.2. The friction force increases with increasing

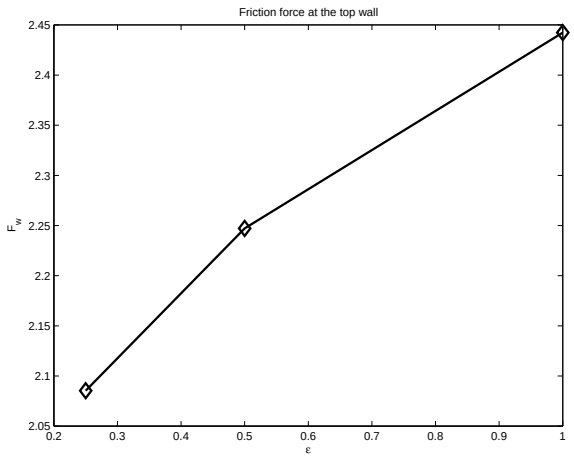

Figure 5.14: Hydroynamic friction force as a function the asperity height.

asperity height, which can be attributed to the increasing horizontal velocity gradient at the top wall, as can be seen in figures 5.9a, 5.10a and 5.11a. Thus, the hydrodynamic friction force shows the expected asperity height dependence.

5.3.3 Influence on the calculation time

For all asperity heights, the number of collocation points is constant, which implies that the overall calculation speed only depends on the number of iterations needed to reach a converged solution; all the other computations are related to the discretization of the geometry and the computation of A and B matrix components and the number of these computations solely depends on the number of collocation points. The number of iterations to reach convergence is displayed in figure 5.15. The figure shows a slight increase in the number of iterations needed to reach a converged solution for increasing values of ϵ: multiplying the asperity height by a factor four, from $\epsilon = \frac{1}{4}$ to $\epsilon = 1$, leads to a multiplication of the number of iterations by less than a factor 1.5, which implies that the increase in the calculation time is relatively small.

5.4 Geometrical limitations

In this section, the outcome of calculations on more complex geometries are discussed. The first modification to the single asperity problem from the previous sections, is the addition of another asperity at the center of the

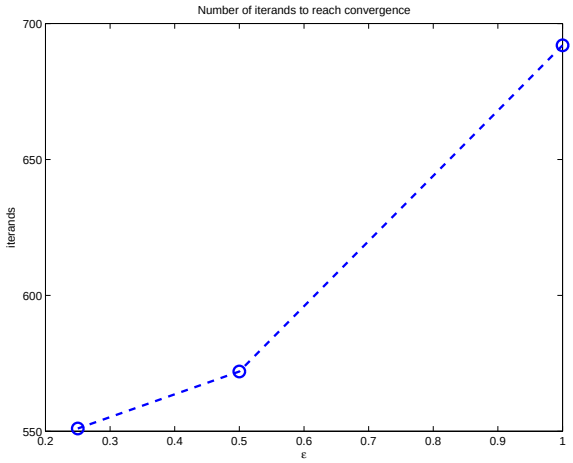

Figure 5.15: Convergence speed as a function of the asperity height.

bottom wall, whereas the second modification leads to a geometry in which three asperities are distributed over the entire bottom wall. The double and triple asperity geometries are shown in figures 5.16a and 5.16b.

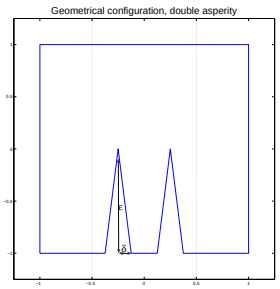

(a) Double asperity.

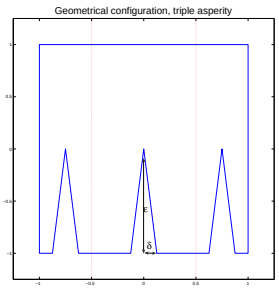

(b) Triple asperity.

Figure 5.16: Sketch of the double and triple asperity domains.

For asperities of half-width $\delta = 2^{-3}$ and 128 collocation points, the left and right boundary velocity as well as the top and bottom wall traction are calculated from the specified quantities, which are identical to the boundary conditions formulated in section 5.1. For every asperity height ϵ, the number of iterations needed to reach convergence is compared to the number of iterations for a single asperity of the same height, as can be seen in figure 5.17. From figure 5.17, it can be seen that a more complex geometry leads to a significant increase in the number of iterations, implying increasing

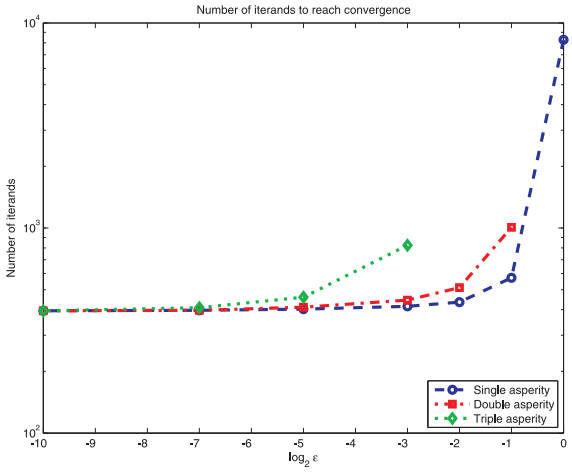

Figure 5.17: Convergence speed for the single, double and triple asperity geometries.

calculation times. Moreover, for larger values of ϵ, convergence could not be reached within the specified maximum number of iteration steps. In fact, the final residuals for these cases tended towards infinity, implying that increasing the specified maximum number of iteration steps will never lead to a converged solution. At the beginning of this chapter, it has been established that increasing the number of collocation points leads to an increase in the number of iteration steps, whereas using less than 32 points for the bottom wall would cause inadequate modeling of the three asperities. Thus, the numerical accuracy can not be used as an instrument to guarantee convergence. This is a disappointing result, as the triple asperity geometry in particular served as first step towards domains with a full length bottom wall roughness.

For the triple asperity geometry with asperities of height $\epsilon = 2^{-3}$ and width $\delta = 2^{-3}$, the horizontal and vertical velocity components show similar behavior near the asperity corners as observed in the single asperity domain, which is shown in figures 5.18a and 5.18b. In analogy to the single asperity domain, the corner effects near the left and right boundaries increase as the asperity height increases. This eventually leads to boundary velocity profiles that are dominated by the influence of the asperity corners, which causes the iterative solver to compute diverging solutions.

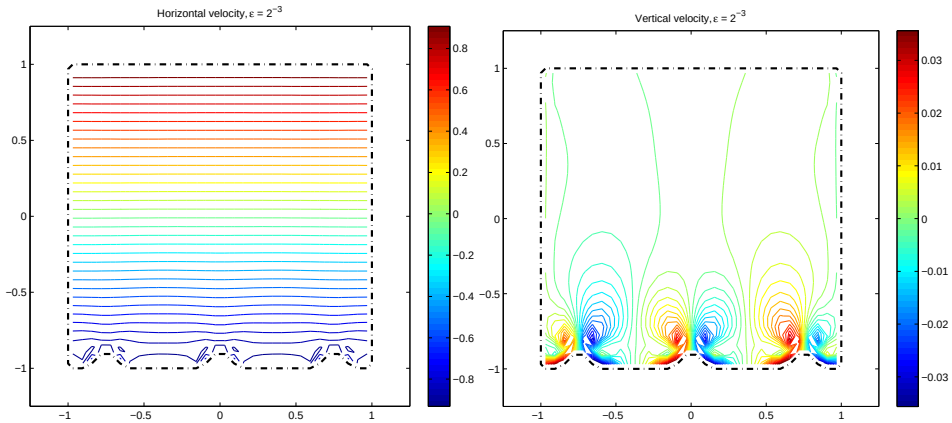

(a) Horizontal velocity. (b) Vertical velocity.

Figure 5.18: Domain plots of the horizontal and vertical velocity.

Chapter 6

Conclusions and recommendations

A boundary integral method for the calculation of Stokes flow in microscopic domains has been developed. It has been established that the Stokes equations apply to the problem of microgeometry friction in deep drawing processes. A boundary integral formulation for the Stokes problem has been derived and converted to a discrete form, which has been implemented into a numerical scheme.

6.1 Validation

The code has been validated by calculating the flow between two parallel, flat walls in opposite motion and comparing the results to the theoretical result known as Couette flow. The code has proven to calculate the boundary velocity profiles properly and it has been confirmed that the singular integrals are treated appropriately, since the accuracy of the results increases with increasing numerical accuracy.

The calculation of the traction is less flawless: for a constant number of points around the corners of the boundary, the traction is calculated improperly, for the other points the results are accurate. The corner inaccuracies are probably caused by numerical inaccuracies arising from the discontinuities in the boundary, as the collocation points for which the traction is incorrectly computed do not form a range of constant length. However, increasing the number of collocation points improves the accuracy of the calculated traction as well.

Although the accuracy of the solution increases with increasing numerical accuracy, this goes at the cost of calculation speed: in addition to the overall number of computations, the number of iterations needed to reach a converged solution rapidly increases with increasing number of points.

6.2 Simulations

The validated code has been used to calculate the flow between two parallel, oppositely moving walls of which one is flat and the other has a single asperity. The calculated solutions have shown converging behavior for an increasing numerical accuracy. Moreover, the influence of the asperity dimensions on the velocity field and the hydrodynamic friction has been investigated. Both the friction and the maximum velocity have shown to increase for increasing asperity height. The calculation time, has shown a slight increase for increasing asperity heights.

Finally, a brief study on more complex geometries has been performed; this study has shown that for a larger number of asperities, a converged solution is not always reached. In particular, for a geometry with asperities positioned close to the corners, the iterative solver produced diverging iterands for larger asperity heights. It may be necessary to use a different iterative solver to overcome this problem; a different possibility is to use a discretization algorithm that approximates the corners by smooth curves, so that the normal vector is well-defined anywhere on the boundary.

6.3 Future perspectives

Recalling the initial concept of modeling the workpiece metal as a highly viscous fluid, an extension towards a two-fluid model can be of interest. As a first step, the tool can still be considered flat and infinitely hard, as can the bulk of the workpiece, since the overall thickness of the workpiece is much larger than the typical roughness height. The geometry thus obtained is schematically displayed in figure 6.1. In order to compute the behavior

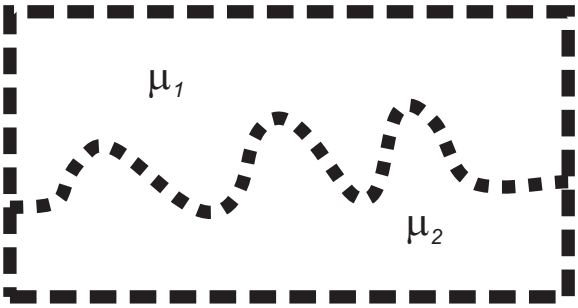

Figure 6.1: Sketch of the two-fluid domain.

of the interface in the middle of the domain, the domain has to be divided into two smaller domains, of which the interface is part of the boundary. Since initially both the traction and velocity of the interface are unknown, an iterative method has to be designed which, for instance, starts with an

initial approximation for the velocity of the interface in the upper domain, which is subsequently used in the lower domain to calculate the traction of the interface. This traction can then be used to update the velocity of the interface by substituting it into the upper domain and so on, until both the consecutive velocity and traction iterands have converged to a certain solution. The full behavior of the interface is then known. A sketch of the divided geometry is captured in figure 6.2. For the lubricant viscosity μ_1,

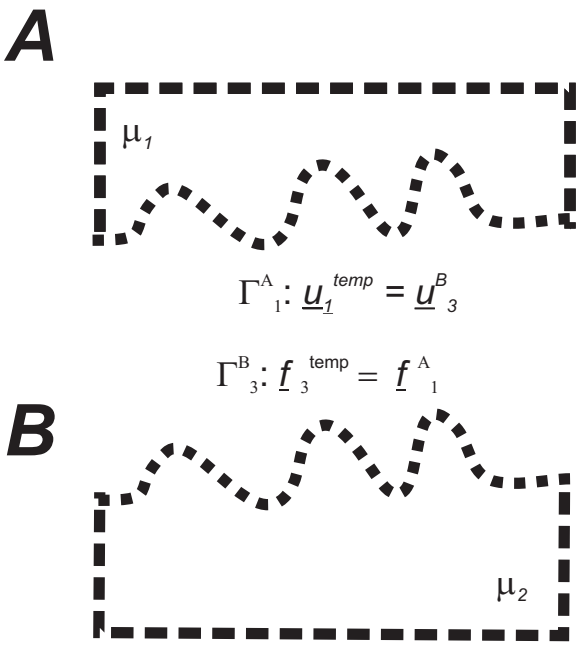

Figure 6.2: Sketch of the divided two-fluid domain.

the experimental values from chapter 2 can be used; for the workpiece viscosity μ_2, an expression must be obtained that represents the hardness of the workpiece material as a viscosity. As stated in chapter 5, the exact boundary conditions are unknown as parts of the boundary are not flat; therefore, the Couette boundary conditions may again be used as an approximation.

All in all, the validation and simulation results look very promising: theoretically expected results (Couette flow) are accurately computed by the code and calculations on the flow in a domains with a single asperity lead to numerically stable results. However, for more complex geometries the iterative solver does not reach a converged solution; therefore, the solution algorithm is the first point of interest for further development towards the modeling of geometrically complex domains.

Bibliography

[1] B. Bhushan and B.K. Gupta. *Handbook of Tribology: materials, coatings and surface treatments.* McGraw-Hill, 1991.

[2] B.N.J. Persson. *Sliding Friction: Physical Principles and Applications.* Springer, 1997.

[3] M.E. Langezaal. Friction prediction by micro geometry modelling. Master's thesis, Delft University of Technology & Corus RD&T, 2006.

[4] J.D. Westeneng. *Modelling of contact and friction in deep drawing processes.* PhD thesis, Univeristy of Twente, 2001.

[5] B.J. Brasjen. Modelling friction in mixed lubricated processes, 2007.

[6] D.J. Schipper. *Transitions in the Lubrication of Concentrated Contacts.* PhD thesis, University of Twente, 1988.

[7] C. Pozrikidis. *Boundary integral and singularity methods for linearized viscous flow.* Cambridge University Press, 1992.

[8] C. Pozrikidis. *A Practical Guide To Boundary Element Methods.* Chapman & Hall/CRC, 2002.

[9] H. Brenner J. Happel. *Low Reynolds number hydrodynamics.* Noordhoff International Publishing, 1973.

[10] C. Pozrikidis. *Fluid Dynamics.* Kluwer Academic Publishers, 2001.

[11] W.C. Emmens. *Tribology of flat contacts and its application in deep drawing.* PhD thesis, University of Twente, 1999.

[12] H.A. Lorentz. Eene algemeene stelling omtrent de beweging eener vloeistof met wrijving en eenige daaruit afgeleide gevolgen. *Zittingsverslag van de Koninklijke Academie van Wetenschappen te Amsterdam*, 5:168–175, 1896.

[13] O.A. Ladyzhenskaya. *The Mathematical Theory of Viscous Incompressible Flow.* Gordon & Breach, 1963.

[14] J.J.L. Higdon. Stokes flow in arbitrary two-dimensional domains: shear flow over ridges and cavities. *Journal of Fluid Mechanics*, 159:195–226, 1985.

[15] B. Carnahan, H.A. Luther, and J.O. Wilkes. *Applied numerical methods*. Wiley, 1969.

[16] E.M. Toose. *Simulation of the deformation of non-Newtonian drops in a viscous flow*. PhD thesis, University of Twente, 1997.

[17] R. Barret et al. *Templates for the solutions of linear systems: Building Blocks for Iterative Methods*. SIAM, 1994.